SAPIENZA
UNIVERSITÀ DI ROMA

Study and optimization of the light-yield of a triple-GEM detector

TESI DI LAUREA MAGISTRALE

FACOLTÀ DI SCIENZE MATEMATICHE FISICHE E NATURALI
CORSO DI LAUREA IN FISICA

Relatore:
Davide Pinci
Relatore Esterno
Giovanni Mazzitelli

Candidato:
Roberto Campagnola
matricola 1032486

A/A 2017/2018

Inside of a ring or out, ain't
nothing wrong with going down.
It's staying down that's wrong.

Muhammad Ali

They who dream by day are
cognizant of many things which
escape those who dream only by
night.

Edgar Allan Poe
"Eleonora", 1841

It's evolution, baby!

Pearl Jam
"Do the Evolution"
***YIELD** ,1998*

A noi tre

Contents

Contents

Introduction

The high-resolution tracking of low energy release particles had a remarkable development in recent years and will give a crucial contribution in different fields, from medical uses to those in dark matter search.

Characteristics, such as high space and time resolution, low material budget, large volumes, low costs, make gas detectors ideal candidates for this type of devices. A very promising technique involves the optical reading of the light produced by the de-excitation of gas molecules during the processes of electron multiplication. This type of detector has been made possible thanks to the great progresses achieved in last years in the performance in micro pattern gas detector and in the evolution of the CMOS technology which led to the production of sensors able of offering high sensitivity and granularity combined with a very low noise level. In this thesis I studied the performance of a prototype where the light is produced through the multiplication of electrons in a triple GEM structure and acquired by a camera equipped with CMOS sensor with 4 Mega Pixels.

Using a high light yield $HeCF_4$ gas mixture, the tracks of alpha particle, emitted by a ^{55}Fe radioactive source, had been revealed.

The thesis is subdivided into five parts:

Chapter 1: Description of all the working principles of particle gas detectors with more detail on processes occurring in GEM gas electron multiplies and in gas scintillation;

Chapter 2: Description in general terms on photo-sensors based on CMOS tecnology;

Chapter 3: Detailed description of the main features of ORANGE prototypes. The optical system was studied and optimized to efficiently collect the produced light;

Chapter 4: Description and analysis of tests performed in laboratory. The detector electronic gain was measured as a function of GEM high voltage supplied.

Chapter 1

Gas Electron Multiplication

The electromagnetic interaction of particle with matter is the one most involved in physical phenomena that occur in gas detectors. The Coulomb interaction is the dominant process that causes the ionization and the excitation of the molecules of the medium. The other electromagnetic interactions (Bremsstrahlung, Cherenkov radiation,..) contribute little to the total released energy. The main processes occurring in gas detectors after the crossing of charged particles are summarized in this chapter.

1.1 Ionization in matter

A charged fast particle passing in a medium releases energy to atoms and molecules. The incident particle, which has charge ze, mass m and velocity v, travels in the medium and sees the electrons move with velocity $-v$, in its reference frame.

Considering an electron at a distance b from the particle trajectory, see fig. 1.1, the transferred momentum will be $\vec{p_e} = \int e \cdot \vec{E}$ and, since the longitudinal component is canceled for symmetry, the transverse component remains:

$$p_e = \int e \cdot E_\perp dt = \frac{e}{v} \int E_\perp dx. \tag{1.1}$$

At this momentum it corresponds, in non-relativistic approximation, an energy transferred to the electron of medium:

$$T_e = \frac{p_e^2}{2m_e} = \left(\frac{ze^2}{4\pi\epsilon_0 b}\right)^2 \frac{2}{m_e v^2} = 2m_e c^2 \frac{z^2}{\beta^2} \frac{r_e^2}{b^2}, \tag{1.2}$$

with $r_e = e^2/4\pi\epsilon_0 m_e c^2 = 2.8fm$ the classical radius of electron and $\beta = v/c$.

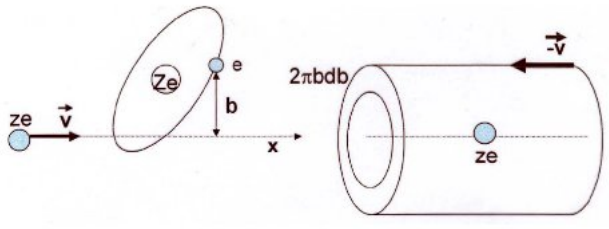

Figure 1.1: Interaction between an incident particle and electron (left); cylindrical ring volume of electrons seen by incident particle (right)

The probability dw that one particle undergoes a collision in a unit path between b and $b + db$ is $dw = 2\pi bdb$ and, using the 1.2 formula, we have:

$$\frac{dw}{dT_e} = 2\pi r_e^2 m_e c^2 n_e \frac{z^2}{\beta^2}\frac{1}{T_e^2} \tag{1.3}$$

For the total energy transferred in a path dx, we must multiply the energy transferred per collision by the corresponding cylindrical ring volume, $2\pi dbdx$, and by the electron density n_e:

$$\frac{d^2E}{dxdb} = -4\pi n_e m_e c^2 \frac{z^2}{\beta^2}\frac{r_e^2}{b} \tag{1.4}$$

that integrated on b between b_m and b_M becomes:

$$-\frac{dE}{dx} = 4\pi n_e r_e^2 m_e c^2 \frac{z^2}{\beta^2}\int_{b_m}^{b_M}\frac{db}{b} \tag{1.5}$$

where b_m, for the uncertainty principle, represents best measurement of the position for a variation of the pulse p_e, $b_m = \frac{\hbar}{p_e} = \frac{\hbar}{m_e c\beta\gamma}$, and b_M taking in to account that the collision time must to be lower than the revolution time of electron, $b_M \simeq \frac{v\gamma}{\omega_e} = \frac{\beta c\gamma}{\omega_e}$.

Inserting this value in the equation 1.5 we obtain the Bohr formula:

$$-\frac{dE}{dx} = 4\pi n_e r_e^2 m_e c^2 \frac{z^2}{\beta^2} ln\left(\frac{m_e c^2\beta^2\gamma^2}{\hbar\omega_e}\right) = 4\pi\frac{N_A Z\rho}{A} r_e^2 m_e c^2 \frac{z^2}{\beta^2} ln\left(\frac{m_e c^2\beta^2\gamma^2}{\hbar\omega_e}\right) \tag{1.6}$$

where $n_e = \rho\frac{N_A Z}{A}$, N_A is the Avogadro number, Z the atomic number, A the atomic weight and ρ the electron density in the matter traversed.

If the incident particles are electrons, the Bethe e Block formula must be modified taking into account the identity between projectile and target. As

a result of elastic collision with the nucleus, the acceleration that a particle undergoes when it is deflected causes the emission of electromagnetic radiation and the acceleration will be as greater as smaller the particle mass is. To the Bethe and Block formula another term that takes into account the energy losses due to radiation would add:

$$\Big(-dE/dx\Big)_{rad} \simeq \frac{E}{X_0} \simeq 4r_e^2\alpha\frac{N_A Z^2\rho}{A}ln(183Z^{-1/3})E \tag{1.7}$$

Since these losses are linear in E, when E increases the radiative contribution will be greater than the ionization, which tends to become constant.

1.1.1 Ionization in gaseous medium

A charged particle that passes through a layer of a gas can release a track of ionization along its trajectory, producing ion-electron pairs. In this case it is possible to write the Bhete e Bloch formula as:

$$-\frac{dE}{dx} = k\frac{Zz}{A}\rho\frac{1}{\beta^2}\Big(ln\frac{2m_e c^2\beta^2\gamma^2 E_m}{I^2} - 2\beta^2\Big), \qquad k = \frac{2\pi N_A z^2 e^4}{m_e c^2}. \tag{1.8}$$

where $m_e c^2$ is the rest energy of the electron, z the charge of the travelling particle, β the velocity of the travelling particle in term of the light velocity c, $\gamma^2 = 1/(1-\beta^2)$, I is the ionization potential of the medium (where $I = I_0 \cdot Z$ and $I_0 = 11.6eV$) and E_m is the maximum of the energy lost in a single collision:

$$E_m = \frac{2m_e c^2\beta^2}{1-\beta^2}. \tag{1.9}$$

From this formula we can say that:

- the energy loss does not depend on the different material properties,neglecting the logarithmic dependence on I;
- for small β, the energy loss goes as $1/\beta^2$, then moves to the minimum and increases logarithmically when $\beta\gamma = \frac{p}{Mc} > 3$.
- the value of $\beta\gamma$, that corresponds to the minimum, depends weakly on I (see fig. 1.2).
- the energy loss is proportional to the square of the particle charge;
- the mass of the incident particle comes into play only by $\beta\gamma = \frac{p}{Mc}$.

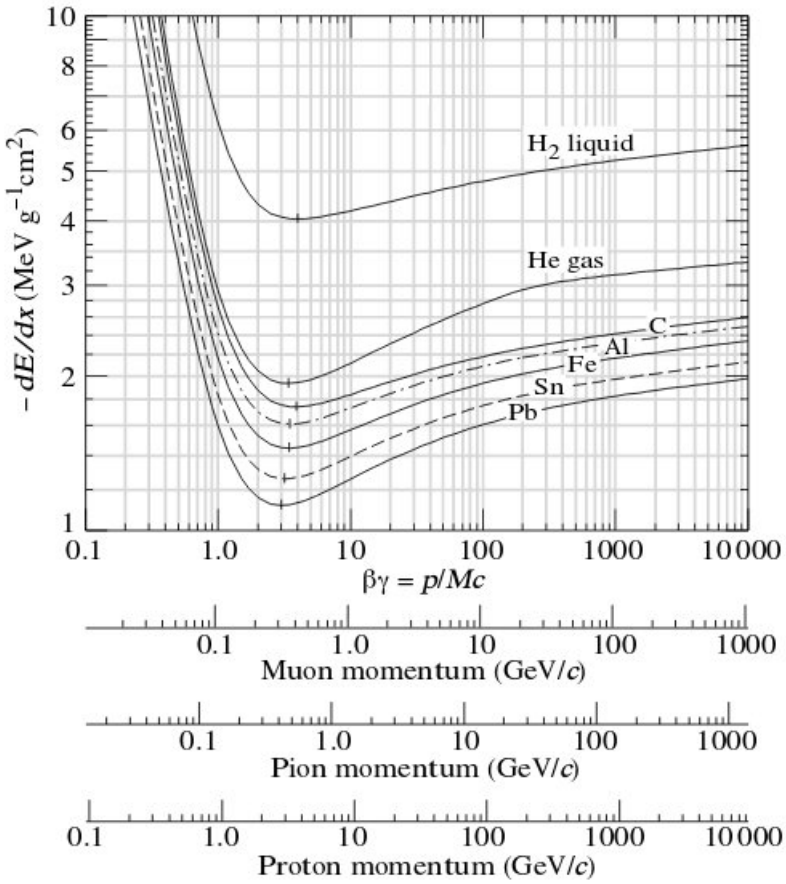

Figure 1.2: Mean energy loss rate in liquid (bubble chamber) hydrogen, gaseous helium, carbon, aluminum, iron, tin, and lead.

The Bhete Block formula takes into account the energy losses in all energetic processes: from simple atomic excitation (big impact parameter) to the transfer of energy to the electrons, δ rays (small impact parameter). The total amount of energy loss can be described by:

$$W < N_I >= L < \frac{dE}{dx} > \tag{1.10}$$

where W, is the average energy that is necessary to create a free electron [1], $< N_I >$ is the average number of ionized electrons along the trajectory of length L.

Interactions with the atoms of the gas are random and characterized by a mean free flight path λ which is given by the ratio [1]:

$$\lambda = 1/(\rho_0 \sigma) \tag{1.11}$$

where ρ_0 is density of target and σ the ionization cross-section. The number of interactions that can occur in a length L has a Poisson distribution, with mean equal to $n = L/l$:

$$P(n,k) = \frac{(n)^k}{k!} e^{-n}. \tag{1.12}$$

.

1.1.2 Ionization in the presence of electric field

If an electric field is applied on gas, electrons and ions move on the field lines and, along these, they are scattered by the gas molecules. For a particle with charge q and mass m, in a medium with an electric field E, we have [15]:

$$m\Big(\frac{dv}{dt}\Big) = qE - kv \tag{1.13}$$

where $-kv$ represents the friction force proportional to the particle velocity. The constant k can be written as $k = \frac{m}{\tau}$, in which τ defines the average time between two collisions (Towsend). When $t > \tau$ the term $-kv$ can be neglected and the equation presents a constant solution:

$$v = \frac{q\tau}{m} E = \mu E, \qquad \frac{dv}{dt} = 0 \tag{1.14}$$

With μ defined as the charge mobility, inversely proportional to the particle mass and directly proportional to τ and to the charge of particle.

1.1.3 Electrons

Because of their light mass, the emitted electrons scatter isotropically and, after collisions, their velocity will have a component with average value equal to zero in all directions, to this the velocity towards the electric field E is added.

Staring by the formula 1.14 (on left), that defines the *average drift velocity* and, writing $1/\tau = u/\lambda = u\rho\sigma$, we have:

$$v = \Big(\frac{e}{m\sigma u}\Big)\frac{E}{\rho}. \tag{1.15}$$

The term E/ρ is the reduced field, u is the instantaneous velocity of the electrons and σ is the cross section between the electron and the gas molecule that depends by the electron energy $\epsilon \rightarrow \sigma = \sigma(\epsilon)$.

Particles crossing the medium are allowed to collide with nuclei through coulombian elastic collision. In each collision the direction of motion changes and, after many interactions, the new direction will be the result of many small deflections.

The cross section that describes the single collision is given by the Rutherford

$$\frac{d\sigma}{d\Omega} = z^2 Z^2 r_e^2 \frac{mc}{p\beta}\frac{1}{4sin^4\left(\theta/2\right)} \tag{1.16}$$

but, in case of a high number of collision, the process is explained with the multiple scattering, where the exit angle θ of the particle will have a Gaussian distribution

$$P\left(\theta\right) = \frac{2\theta}{<\theta^2>}e^{-\frac{2\theta^2}{<\theta^2>}}d\theta \tag{1.17}$$

with fluctuation equal to

$$\theta_{rms} = \sqrt{<\theta^2>} = \frac{21MeV/c}{p\beta c}\sqrt{\frac{x}{X_0}} \tag{1.18}$$

in which p is the particle momentum, x is the traversed thick and X_0 is the radiation length. In both the direction orthogonal to the particle velocity becomes:

$$P\left(\theta_y\right)d\Omega = \frac{1}{\sqrt{2\pi <\theta_y^2>}}e^{-\frac{\theta_y^2}{<\theta_y^2>}}d\theta_y \tag{1.19}$$

with the corresponding fluctuation:

$$\theta_y^{rms} = \sqrt{0.5 <\theta^2>} = \frac{13.6MeV/c}{p\beta c}\sqrt{\frac{x}{X_0}}. \tag{1.20}$$

1.1.4 Ions

The ions drifting differs from electrons' because of their larger mass. Good fraction of the energy is lost in the collision and momentum of the ions is not randomized. The ions drift velocity is defined as:

$$v^+ = \mu^+ \frac{E}{\rho} \tag{1.21}$$

where μ is the ions mobility, which is specific for each gas, and E/ρ is the reduced field. The mobility and the diffusion coefficient are linked by the Nernst-Towsend formula (or Einstein formula) by:

$$\frac{D}{\mu} = \frac{kT}{e} \tag{1.22}$$

which is, in the ions case, a constant. This characteristic is given by the constant average energy of the ions in the gas.

For a gas mixture the mobility μ_i^+ of the ion G_i^+ can be evaluated by the Blanc's law:

$$\frac{1}{\mu_i^+} = \sum_{j=1}^{n} \frac{p_j}{\mu_{ij}^+} \tag{1.23}$$

where p_j is the gas concentration j in a volume and μ_{ij}^+ is the mobility of the ion G_i^+ in the gas G_j [1].

A new ion is created when the migrating ions hit molecules with a ionization potential smaller than the energy available in the ion, leading to a charge exchange process and to the neutralization of the ion. The rate of ions transformation through charge transfer is high and proportional to the concentration of the molecules to be ionized, due to the cross section that are of a similar order of magnitude to other ion-molecule scattering cross-sections.

Electron Diffusion

When the drifting electrons are scattered on a gas molecules, their velocities change from the average. In the simplest case, the deviations are the same in all directions and if the process begins with a point-like cloud of electrons, at a time $t = 0$ in the origin of the system along the direction z, after some time t, the cloud will assume a Gaussian density distribution:

$$n = \left(\frac{1}{\sqrt{4\pi Dt}}\right)^3 e^{\frac{-r^2}{4Dt}} \tag{1.24}$$

where $r^2 = x^2 + y^2 + (z - vt)^2$ and D is the diffusion constant. By the microscopic interpretation, starting from the equation 1.22 and writing the average thermal energy as $\epsilon = 3/2kT$, we can write D as:

$$D = \frac{2}{3}\frac{\epsilon}{m}\tau \tag{1.25}$$

and remembering that $\mu = \frac{e}{m}\tau$, we can find the electron energy measuring the ratio D/μ:

$$\epsilon = \frac{3}{2}\frac{De}{\mu}. \tag{1.26}$$

The energy defines the diffusion width σ_x of an electron cloud which, after starting point-like, has travelled over distance L:

$$\sigma_x^2 = 2Dt = \frac{2DL}{\mu E} = \frac{4\epsilon L}{3eE}. \tag{1.27}$$

Experimentally the value of the electron diffusion along the electric field can be quite different from that in the perpendicular direction. We know that the diffusion of the drifting ions is non-isotropic: when the ions collide with the gas molecules, they retain the direction of the motion along the electric field because the partners of the collision is similar. Results that the diffusion is larger in the drift direction.

For the electrons, restricting the study to energy loss by elastic collisions, we consider the mobility. The mobility of electron assumes different value along the edge and in the center of the travelling cloud. This change of mobility inside the cloud corresponds to a change of diffusion in the longitudinal direction; the diffusion in the perpendicular direction also change. Introducing the two diffusion coefficients related to longitudinal (D_L) and perpendicular (D_T) diffusion, the distribution density in the anisotropic case becomes [15]:

$$n = \frac{1}{\sqrt{4\pi D_L t}}\Big(\frac{1}{\sqrt{4\pi D_T t}}\Big)^2 e^{\left[-\frac{x^2+y^2}{4D_T t} - \frac{(z-vt)^2}{4D_L t}\right]}. \tag{1.28}$$

High electric fields

The increase of the electric field above some keV/cm leads to an increasing number of ionized electrons that have the energy to produce inelastic phenomenons when collide with molecules: ionizations and excitations.

If the electron emitted has an energy equal to the first ionization potential of the gas molecule, it may create an electron ion pair and it can lead

to multiplication process. Two different types of ionization can take place: primary and secondary, fig. 1.3.

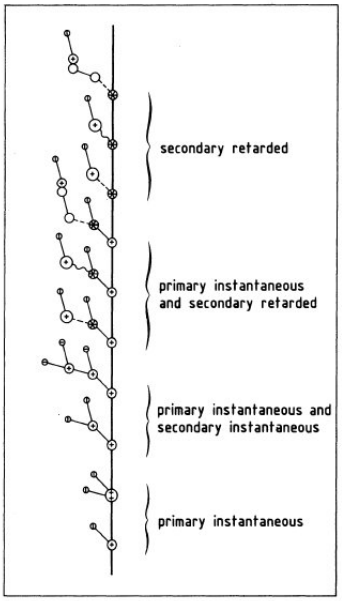

Figure 1.3: Emission of primary and secondary electrons along the path of the ionizing particle.

The primary ionization is one in which, one or more electrons are ejected from the molecules by the crossing particle. The secondary electrons are usually created in the immediate proximity of the primary encounter and, together with the primary electrons, form a structure called clusters of one or several electrons.

Unlike the ions and the electrons, the photons produced by excitation of atomic energetic levels are not influenced by the electric field. They can interact with the gas molecules by the photoelectric interaction that it is possible only when the photons have enough energy to overcome the binding energy to remove the electron from the atom. The typical photon energy is $E_\gamma \ll m_e c^2$, the process can be as

$$\gamma + A \rightarrow e^- + A^+ \tag{1.29}$$

the corresponding cross-section is

$$\sigma_{p.e.} \propto Z^5 \frac{1}{E_\gamma} \tag{1.30}$$

and it depends strongly by the atomic number of the material, [4].

1.2 Gas electron multipliers

The Gas Electron Multiplier, GEM [16], is a micro-pattern gas detector that can be used for the high resolution particle tracking. By means of this device the electrons, produced in a gas mixture by a ionizing particles, are multiplied within the GEM channels where a high electric field is present.

1.2.1 Standard single GEM

The standard GEM is a kapton foil with a thickness of about 50 μm, clad on each side with a thin copper layer (5 μm) and perforated with holes with a high surface density. The holes have a bi-conical shape with a diameter ranging from 50 μm to 70 μm. In fig. 1.4 it is possible to see a foil magnification and, in fig. 1.5, the hole cross-section, as seen at electron microscope.

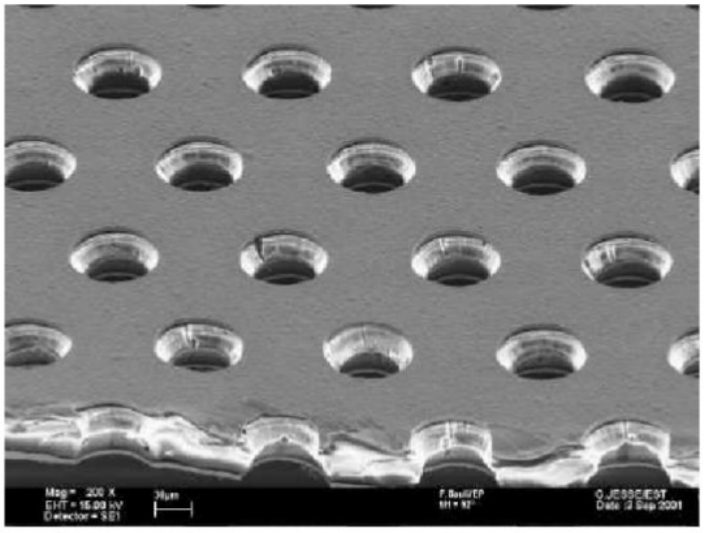

Figure 1.4: GEM foil as seen under at the electron microscope, [2].

It is possible to produce within the holes an electric field of 100 kV/cm, the channel field E_c, by applying a voltage difference of about 500 V between the two copper sides. When a charged particle passes through the gas, ionizes molecules that generate primary electrons. An external electric field, fig. 1.6 drift field E_d, can bring the primary electrons through the GEM and the high field inside the holes induces an avalanche process. In transfer gap, a transfer electric field E_t extract secondary electrons [2], see fig. 1.7.

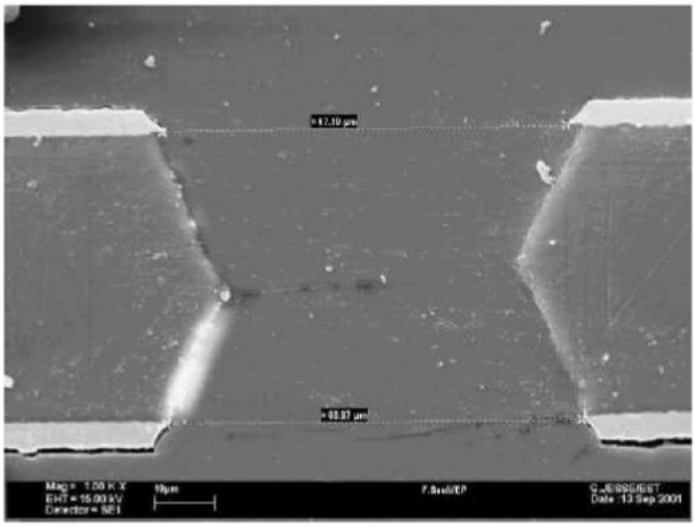

Figure 1.5: GEM hole cross-section as seen at electron microscope, [2]

Figure 1.6: Schematic view of the single sheet GEM.

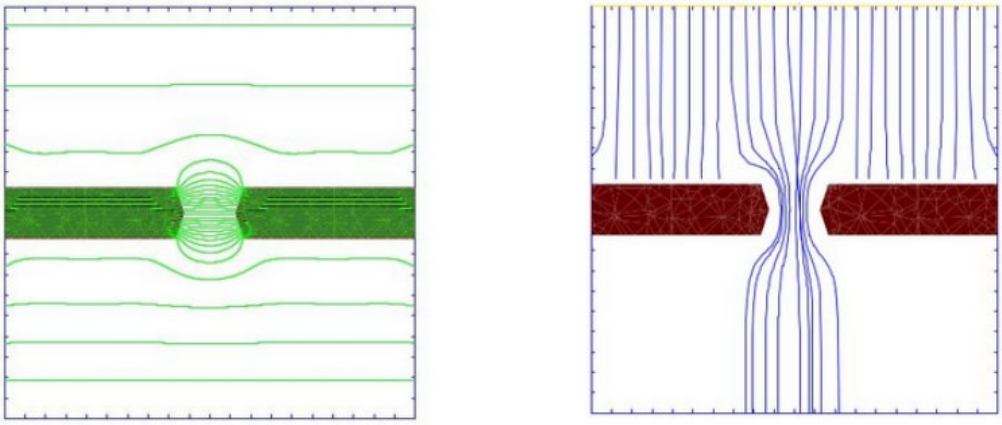

Figure 1.7: Equipotential lines, on the left, and electron drift lines, on the right, in a region of 400×400 μm around the GEM channel, [2].

1.2.2 Standard GEM electron transparency

Because of the diffusion effect and the defocused field lines, some electrons can collide with the upper GEM electrode, as we can see in fig. 1.8. The ratio between the number the electrons entering in the channel and the number of electrons above the GEM is defined as the *collection efficiency*: ϵ_{coll}^{el}.

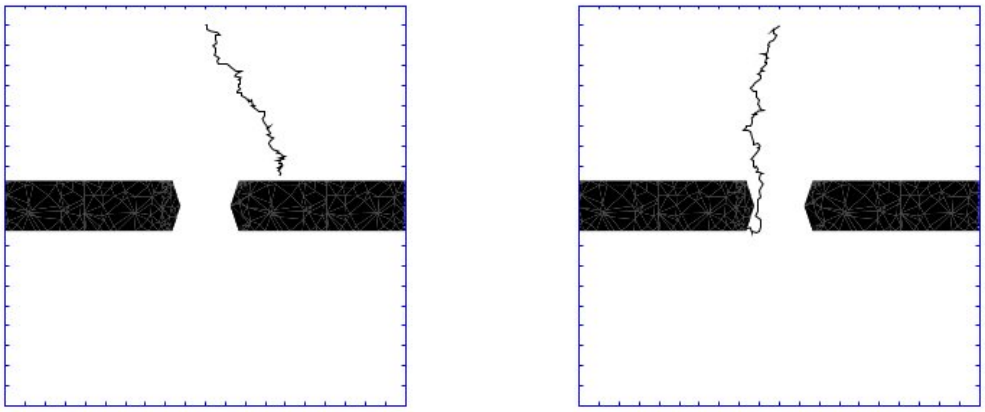

Figure 1.8: On the left, an electron hits the the upper electrode; on the right, an electron is lost inside a GEM channel, [2].

Some electrons are lost on the kapton inside the GEM while others can hit the lower side of the GEM foil due to the poor extraction capability of the electric field below the GEM. The ratio between the number of electrons

extracted and the number of electrons entering in the channel is the *extraction efficiency*: ϵ_{extr}^{el}. The probability that an electron, produced in the drift zone, arrives in the transfer area crossing a channel of the GEM foil, is called *electron transparency*. It is very important for the particle detection: it is a decisive parameter for the energy resolution and directly affects the detection performance,and is defined as

$$T = \epsilon_{coll} \cdot \epsilon_{extr}. \tag{1.31}$$

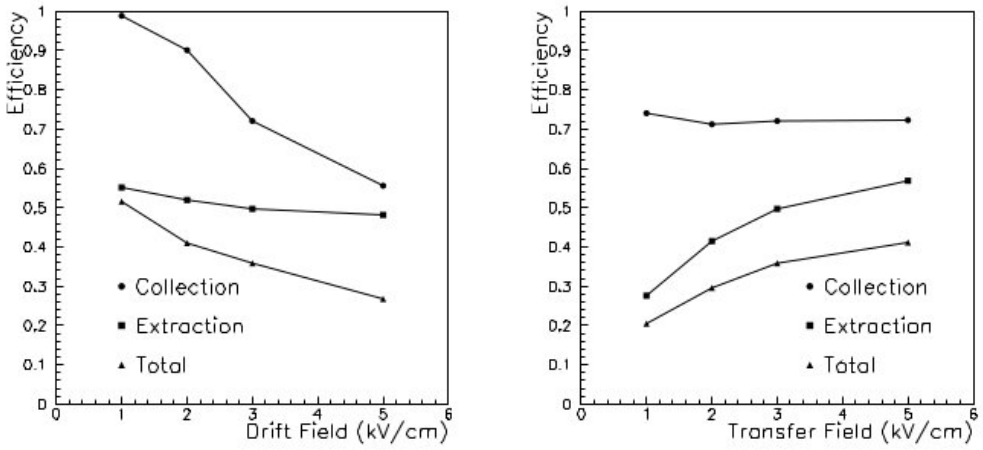

Figure 1.9: Tranparency dependence on drift field, on the left, and on the transfer field, on the right, [2].

Figure 1.9 shows the dependence of the efficiencies on the two electric fields (drift and transfer). When the electric field E_d increases, a large fraction of electrons can hit the upper GEM copper side, causing the decrease of the electron transparency. On the other hand a high electric drift field is necessary to avoid charge losses in the gas through secondary effects, as the recombination. In this figure, it is noted that the ϵ_{coll}^{el} and the transparency (total) decrease at high drift fields due to the defocusing effect, while with a better electron extraction capability the total transparency of the GEM increases at high transfer fields.

1.2.3 Standard GEM gain

When the energies of the incident particle exceed the first ionization potential of the gas molecules, the ion-electron pair production occurs, which is the first step of the avalanche multiplication. The number of pairs produced in

a dx path is linearly proportional to the number of electrons:

$$\frac{dn}{dx} = \alpha(E) \cdot n \tag{1.32}$$

The $\alpha(E)$ is called *first Townsend coefficient* and it is a function of the electric field. The electric field in the channel E_c allows the development of the avalanche: the number of secondary created by primary electrons increases with the increase of E_c, but it reduces the extraction of the secondary electrons affecting the transparency.

If electronegative gases are used, the electron capture process will occur. The associated equation will be:

$$\frac{dn}{dx} = -\eta(E) \cdot n \tag{1.33}$$

where $\eta(E)$ is called *attachment coefficient.*

The gain for a single electron drifting from x_1 to x_2 results from the above equations:

$$G_{single} = exp\Big(\int_{x_1}^{x_2} [\alpha(E) - \eta(E)]dx\Big) \tag{1.34}$$

which takes in to account both the effects: if the field in the channel is sufficiently high the attachment effect can be neglected with respect to the multiplication; the drift lines are concentrated near the channel axis: due to the diffusion effect the electrons can reach the regions close to the kapton where the higher field results in higher multiplication.

The average number of secondary electrons produced per single electron entering into a hole will be indicated as intrinsic gain G_{intr} , while the average number of secondary electrons, extracted from the lower side of the GEM per primary electron generated above the GEM, will be indicated as *effective gain* G:

$$G = G_{intr} \cdot T \tag{1.35}$$

Each single GEM has an effective gain which is an exponential function of the voltage applied:

$$G^{(i)} = A_k e^{\alpha_k V_{gem}^{(i)}} T_{(i)} \tag{1.36}$$

A_k and α_k being dependent on the gas mixture and T depend on the field above and below the GEM.

1.3 Triple-GEM configuration

A triple-GEM detector is device composed by 3 GEM foils inserted between two conductive planes: the cathode, which forms the drift gap above the first

GEM, and the anode, which is usually used as signal readout. The ionization of the gas molecules occurs in the drift gap, the space between the cathode and the first GEM. The regions between the GEM are called *transfer gaps* while the *induction gap* is the gap between the last GEM and the anode, see fig. 1.10.

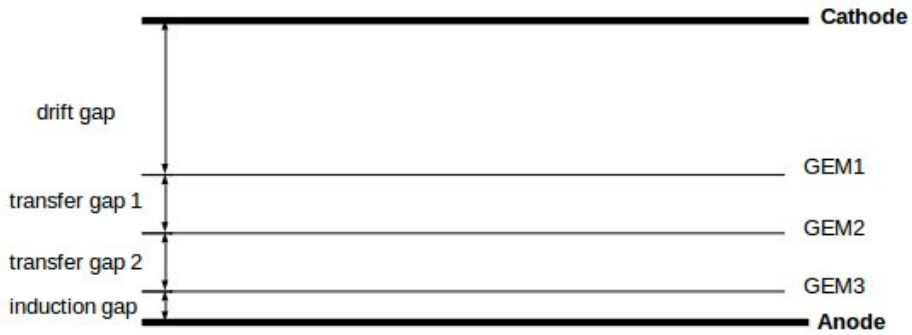

Figure 1.10: Triple-GEM based detector cross-section

Electrons produced in ionization process, reach the first GEM by means of the drift electric field, and then, by means of two transfer electric fields, the electron clouds reach the second and the third GEM. Once the electrons cross the last GEM and reach the induction gap, they give rise to the formation of an induced current signal on the anode. This current is then amplified and shaped by the readout electronics.

In the transfer gaps, the secondary electron clouds are carried out from the first GEM and drifted towards the following one. Therefore, the electric field in the transfer gap (E_t) is an important parameter to be studied and optimized. To ensure a good extraction capability of the secondary electrons from the upper GEM in the transfer gap,a high E_t is required; on the other hand E_t has to be jet low to reduce the defocusing effect, fig. 1.9.

1.3.1 Triple-GEM gain

By analyzing the gain, by adapting the equations found for the single GEM foil in the previous section,an evaluation of the device is possible.

For a system with three GEM sandwiched, the gain is essentially given by:

$$G = G^{(1)} \cdot G^{(2)} \cdot G^{(3)} = A_k^3 \cdot T_1 T_2 T_3 \cdot e^{\alpha_k (V_1 + V_2 + V_3)} \tag{1.37}$$

and results a function of the sum of the all voltage supplies, V_{tot}. The

gain depends on the gas mixture characteristics, on the transparencies (i.e. the electric field configuration) and on the sum of voltage supplies, V_{tot}.

1.3.2 Signal formation

In both single GEM and triple-GEM devices, as soon as the electrons enter into the induction gap, they start to induce on the electrodes a current, which stops when they are completely collected.

The time evolution of the current can be calculated using the Ramo theorem:

"Given any configuration of electrodes $1, ..., j, ..., n$ at different potentials $V_1, ..., V_j, ..., V_n$, the current flowing into an electrode k due to a moving charge q is:

$$I_k = \frac{-q\vec{v}(x) \times \vec{E_k}(x)}{V_k} \tag{1.38}$$

where $\vec{E_k}(x)$ is the electric field created by raising the electrode k to the potential V_k while keeping $V_{j \neq k}$=0", [2].

If V_k= 1 V the resulting electric field is called *weighting field* $\vec{E_k^w}$ and the Ramo theorem become:

$$I_k = -q\vec{v}(x) \times \vec{E_k^w}(x) \tag{1.39}$$

The real electric field is also constant in the gap and then the electron drift velocity is constant too.

The drifting electrons induce a constant current I during the drift process and if q is the charge collected, since

$$\int_{drifttime} I \cdot dt = q, \tag{1.40}$$

the shorter is the drift time the higher the value of I. For this reason the induction gap has to be chosen as thin as possible. In figure 1.11 is possible to see the current induced by one electron on a pad in the last gap.

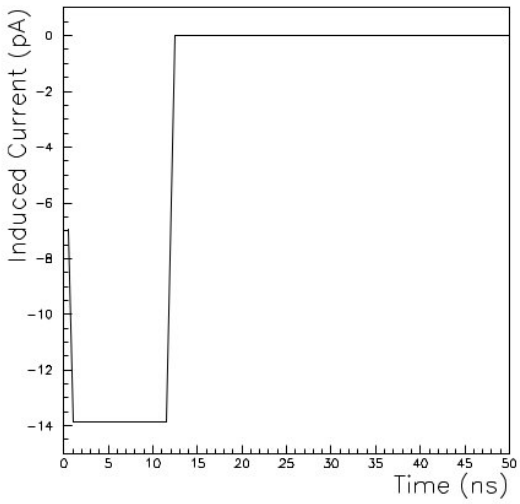

Figure 1.11: Current I induced on a pad by one electron drifting in the last gap as calculated with Ramo theorem, [2].

With a detector based on triple-GEM it is possible to study the phenomena that occur during the ionization process inside the gaseous region crossed by a charged particle. The events readout can be achieved by using the signal induced by the electrons on appropriate electrodes, or collecting the light emitted by the de-excitation of the gas molecules through optical sensors like CCD or CMOS. In this thesis we present the results obtained using both the reading channels, paying greater attention to those obtained by the optical readout of the device.

1.4 PMT

Many detector used in particle physics, nuclear physics and astrophysics are based on γ detection in $100nm \leq \lambda \leq 1000nm$ interval.
γ detection include three stages:

- photoelectron (p.e.), generation from a photon by photoelectric or photoconductive effect;
- p.e. amplification to a detectable level via shower processes;
- electron collection and signal formation.

γ detector main features are:

- Quantum efficiency (QE or ϵ_Q): number of p.e. generated per impinging photon($0 \leq \epsilon_Q \leq 1$ in phototubes)
- collection efficiency (CE or ϵ_C: probability of generated photon being collected;
- gain (G): number of electron collected per photoelectron generated and collected;
- dark current: outgoing current with no impinging photons

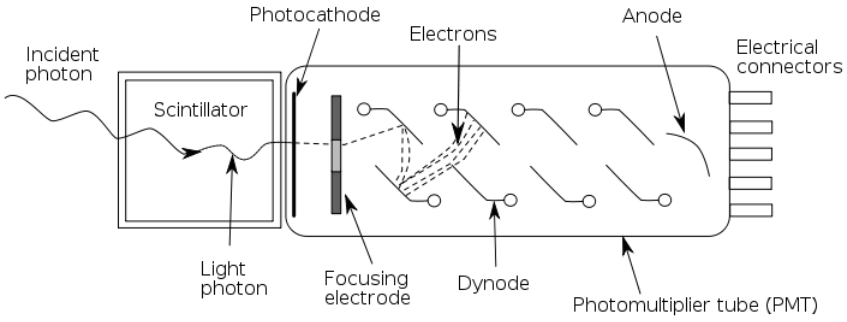

Figure 1.12: Schematic diagram of a photomultiplier tube

The photocathode, hit by a photon of characteristic energy, emits an electron that is later accelerated and collected on the first dynode. Because of the first electron, other electrons are ejected, that are accelerated on the second dynode, where secondary electrons are generated. Via the same processes on the following dynodes, a multiplication process occurs and the total charge is collected on the anode. A proper voltage is needed in order to accelerate the electrons in between the dynodes.
When a photon of energy $h\nu$ above the threshold hits the photocathode,it can extract an electron with energy $E = h\nu - \phi$ with ϕ working function. The quantum efficiency is between 10 and 30% and depends on the photosensitive material and on the impinging photon wavelength.

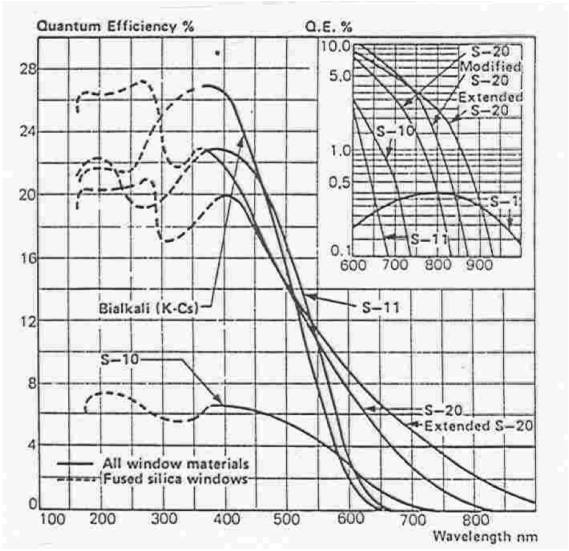

Figure 1.13: Quantum efficiency as a function of impinging photon wavelenght for a PMT

On the metallic dynodes, an alkali metal layer (IA) or an alkali earth metal layer is deposited. When an electron incides on the first dynode, it extracts several number of electrons, δ secondary emission factor. In phototubes 10 ti 14 stage are built, with an amplification up to 10^7.
The number δ of electron produced by the dynode per impinging electron depends on the electron energy and, then, on the d.o.p. between two following dynodes:

$$\delta = KV_d \tag{1.41}$$

and, assuming n dynodes with the same V_d, the gain is:

$$G = \delta^n = (KV_d)^n \tag{1.42}$$

and the applied voltage is:

$$V_b = nV_d = \frac{n}{K} G^{\frac{1}{n}} \tag{1.43}$$

1.4.1 Signal from PMT

The PMT can be considered an ideal current generator:

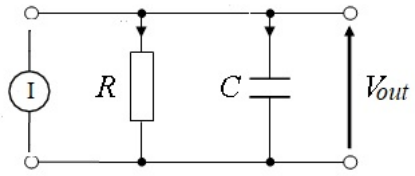

Figure 1.14: Ideal current generator scheme: R output resistance seen by the anode; C anode capacity

The current in the PMT is:

$$I(T) = \frac{GNe}{\tau_s} e^{-\frac{t}{\tau_s}} \tag{1.44}$$

with τ_s signal decay time from scintillator, G gain, N number of photoelectrons, e electron charge.

The circuit equation is:

$$I(t) = \frac{V}{R} + c\frac{dV}{dt} \tag{1.45}$$

with $\tau = RC$. The solution depends on τ compared to τ_s:
if $\tau \neq \tau_s$ we have:

$$V(t) = -\frac{GNeR}{\tau - \tau_s}\left(e^{-\frac{t}{\tau}} - e^{-\frac{t}{\tau_s}}\right) \tag{1.46}$$

If $\tau = \tau_s$

$$V(t) = \frac{GNeR}{\tau - \tau_s} t e^{-\frac{t}{\tau_s}} \tag{1.47}$$

- For $\tau \ll \tau_s$ the signal quickly rises, with $\tau = RC$ as a limit, then drops exponentially with τ_s as constant. The signal is little, and reproduces the de-excitation signal in the scintillator. In this case, called "current mode operation" the signal are fast, fitting for high rate acquisition.

- For $\tau \gg \tau_s$ the signal is integrated by the output circuit and drops exponentially with τ as constant. This is the "voltage mode operation", where the signal are large, but more stable, fluctuation-independent but with a high probability for pile up in case of high rate acquisition.

Chapter 2

CMOS photo-sensor

CMOS photo-sensor, i.e. Complementary Metal Oxide Semiconductor whit a photosensitive element, is a device able to provide the optical readout of the light produced in the triple-GEM structure.

In the simplest form, to collect the light we used the CMOS Active Pixel Sensor (APS) consisting of one photodiode and three Metal Oxide Semiconductor Field Effect Transistor, or MOSFET.

This chapter describes the main features of this type of sensors, starting from some basics.

2.1 Diode and Photodiode

Diodes and photodiodes are devices based on p-n junction connected by two electrical terminals. The p-n junction is a layer between two types of doped semiconductors: n-type and p-type. Starting by a base of tetravalent crystal (as Si or Ge), through different technology, it is possible to insert in the lattice atoms with different valence,i.g.:

- donor atoms with valence 5 (As, P), creating an n-type semiconductor with an excess of free negative charge;
- acceptor atoms with valence 3 (B, Al), creating a p-type semiconductor with a shortage of free negative charge.

Despite the addition of donor-acceptor atoms, the crystal structure continues to be neutral.

When these two types of semiconductor are combined, the negative charges of the n-type tend to reach the p-type zone and the same thing occurs for the positive charges. The moving charges lead to the formation of a potential

barrier W which increases up to that carriers do not have enough energy to overcome. At the equilibrium, by a recombination process, a depletion zone was formed which will lead a charge inversion respect to the starting point, (see fig. 2.1).

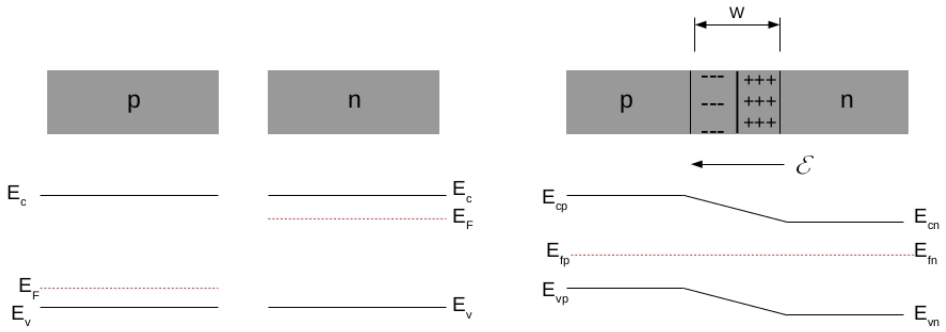

Figure 2.1: Properties of an equilibrium p-n junction: on the left, p-region and n-region isolated and the relative energy bands; on the right, the junction, the space charge in the transition region W, the resulting electric field and the separation of energy bands.

The potential barrier can be modified through the application of an external voltage: the barrier becomes lower with a direct polarization (positive pole in the p-area) or highest with a inverse polarization (positive pole on the n-area).

If an external voltage is applied:

- if the voltage has the same polarity of the build-in potential, the depletion zone behaves like an insulator, not allowing the passage of the current (this is the mode in which the photodiodes works);
- if the external voltage has opposite polarity than the built-in potential, the recombination takes place again generating an electrical current.

In the simplest way, then, we can say that a diode is an electronic component based on p-n junction equipped with two terminals that conducts primarily in one direction; it has low (ideally zero) resistance to the flow of current in one direction, and high (ideally infinite) resistance in the other.

The characteristic $I-V$ curve of an ideal diode is provided by the Shockely equation:

$$I = I_S\left(e^{\frac{eV_D}{kT}} - 1\right) \tag{2.1}$$

where I is the diode current, I_S the reverse bias saturation current, V_D the voltage across the diode, k the Boltzmann constant and T the temperature [19].

In a photodiode, formed by a p-n junction, the photogeneration process (or the photoelectric effect) is involved to the formation of mobile charge carriers. The photogeneration process occurs when a photon, which illuminates a semiconductor, has enough energy $h\nu$ to cause the excitation of an electron from the lower energy valence band to the higher energy conduction band: this process gives rise to the formation of electron and holes.

The operation of a photodiode, then, relies the separation of the photogenerated carriers by the built-in field inside the depletion region of the p-n junction. Under the influence of the built-in electric field, the photogenerated electrons will drift towards the n-side, and photogenerated holes will drift towards the p-side. The photogenerated carriers that reach the quasi-neutral region outside of the depletion layer will generate an electric current flowing from the n-side to the p-side; this current is called a photocurrent.

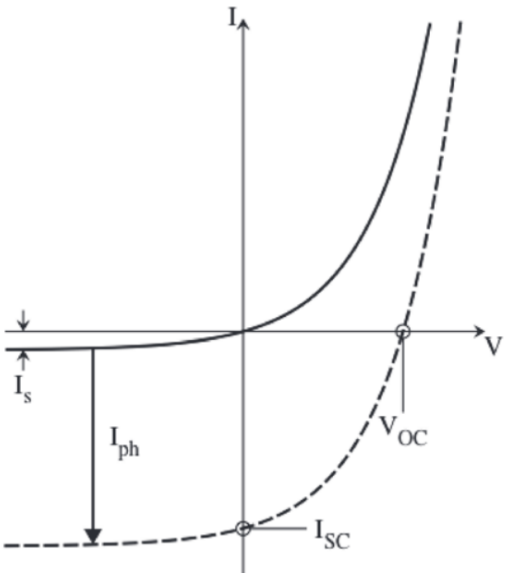

Figure 2.2: $I-V$ characteristic and shifting of the $I-V$ characteristic due to the photogenerated current, I_{ph}, [20].

The generation of the photocurrent results in the shift of the $I-V$ characteristic of the photodiode, fig.2.2. Therefore, the $I-V$ characteristic of a photodiode is expressed as:

$$I_L = I_S[e^{\frac{qV}{kT}} - 1] - I_{ph}, \tag{2.2}$$

in which the first term is the Scottky equation and I_{ph} is the photocurrent.

Analyzing this curve, it is possible to learn that the three different trends characterize the corresponding types of photodiodes: the open circuit mode, short circuit mode and the reverse bias mode, [20].

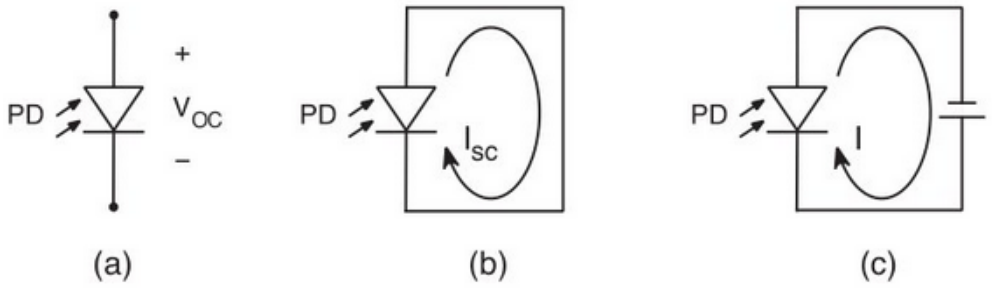

Figure 2.3: (a) open circuit mode, (b) short circuit mode, (c) reverse- bias mode, [20].

- Open circuit mode, fig. 2.3(a), corresponds to a photovoltaic mode: the terminals of the photodiode are connected with open circuit; there is no net current flowing across the photodiode, but due to the photogenerated current; a net voltage is created across the photodiode, called the open circuit voltage, V_{OC}. In fig. 2.2, the photodiode is operating at the point where the $I-V$ characteristic curve intersects the x-axis.

- In the short circuit mode, the terminal of the photodiode is short-circuited. This allows the photogenerated current to flow in a loop as illustrated in fig. 2.3(b). In the fig. 2.2 this is represented by the point at which the $I-V$ characteristic curve intersects the y-axis. The current that flows in the loop in SC mode is also known as the short circuit, I_{SC}, and it has the same magnitude as I_{ph}.

- In reverse bias mode, a reverse bias is applied across the photodiode as shown in fig. 2.3(c), therefore it works in the lower left quadrant of fig. 2.2. By applying a bias voltage, the potential difference across the p-n junction changes to $V_0 - V$, and the balance between drift and diffusion in the p-n junction also changes. This is reflected in the width of the depletion region W .

Operating in reverse bias we have the effect of increasing W and the electric field E. The new depletion region creates a greater photogeneration region, while the stronger E increases the drift velocity of the photogenerated carriers. In this way, the drift velocity increases in proportion with E and the

average time, that a drifting carrier has to reach the end of the depletion region (transit time), is reduced: the signal loss due to recombination in the depletion region is also reduced. This mode is the preferred one for a photodiode.

2.2 MOS and MOSFET devices

The devices called MOS (Metal-Oxide-Semiconductor) and MOSFET (Metal-Oxide-Semiconductor-Field-Effect-Transistor) are based on p-n junction. Inserting a layer of silicon dioxide (SiO_2) between a layer of metal and a doped silicon substrate the traditional MOS structure is obtained. The silicon dioxide is a dielectric material, so its structure is equivalent to a planar capacitor, with one of the electrodes replaced by a semiconductor.

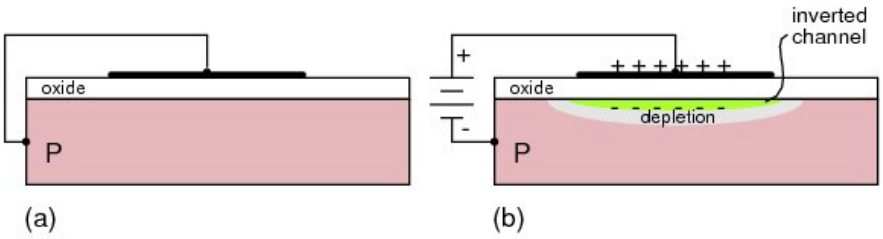

Figure 2.4: Metal-oxide-semiconductor structure on p-type silicon: no charge (a), charged (b), [12].

The distribution of charges in the semiconductor could be modified when a voltage is applied across the MOS structure. If we consider a p-type semiconductor, when a positive voltage is applied, the positive charges move away from the creating depletion layer. If the voltage is high enough, a concentration of negative charge carriers is created near the interface between the semiconductor and the insulator, fig. 2.4.

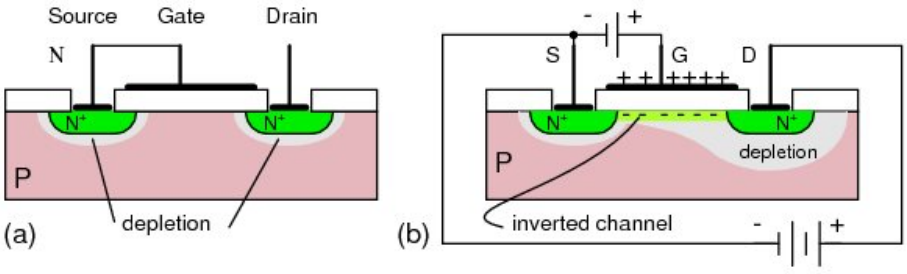

Figure 2.5: N-channel MOSFET (enhancement type): (a) 0 V gate voltage, (b) positive gate bias, [12].

A metal-oxide-semiconductor field-effect transistor is based on the modulation of charge concentration by a MOS capacitance between an electrode and a gate located above and insulated from all other device regions by a dielectric layer which is an oxide, such as silicon dioxide. The MOSFET includes two additional terminals with respect to the MOS capacitor, source and drain, each connected to individual highly doped regions that are separated the body region. These regions must be of the same type,regardless they are either p or n type, and of opposite type to the body region, which is less doped.

There are two types of MOSFET:

- the enhancement MOSFET
- the depletion MOSFET

We describe the enhancement type. The depletion MOSFET can be studied by changing the polarities of the region and the voltages. Figure 2.5 shows a schematic picture of the n-type MOSFET or nMOSFET (enhancement MOSFET). With no bias voltage applied to the gate terminal, there exist two consecutive pn junctions between the drain and source and no current flows from drain to source. When we apply a voltage V_GS between the drain and source, because of the oxide layer under the gate electrode, the gate current will be essentially zero, but two things happen:

- free holes in the p-type substrate are repelled from the region under the gate leaving "uncovers" bound negative charges;
- Electron from the heavily doped N+ regions are attracted under the gate.

These effects create an induced n-type channel: only when the $V_{GS} \neq 0$ the channel is formed, on the other hand under the gate there are not charges. If a voltage V_{DS} is applied between the drain and the source, we will have a flow of electrons from source to drain. The nude acceptors, as we can see in the MOS case, built the inversion channel. Adjusting V_{GS}, it is possible to control the electron density in the channel, and then the current.

In the MOSFET capacitor the inversion layer electrons are supplied very quickly from the source/drain electrodes, unlike the MOS, where they produced slower, through carrier generation and recombination centers in the depletion region.

2.3 Imaging via CMOS circuit

The Active Pixel Sensor, or APS, is a matrix composed by a large number of pixels, in which, for each of them, there are a simplest form of CMOS circuits, composed by a photodiode, an amplifier and different MOSFETs.

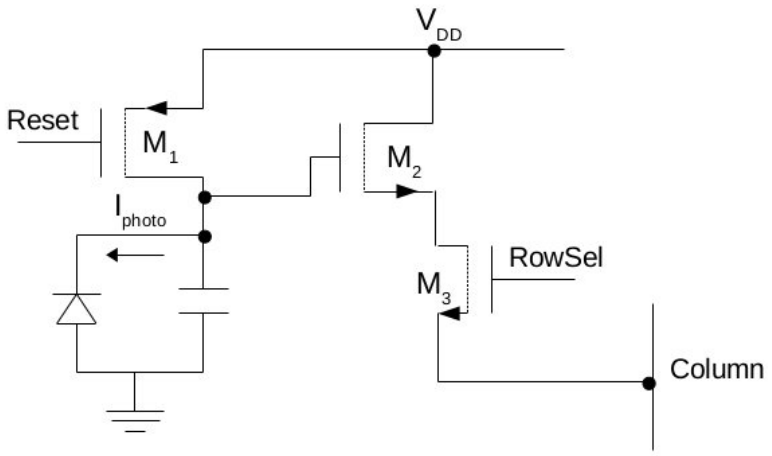

Figure 2.6: 3-Transistor CMOS Active Pixel sensor, [3].

The typical scheme of a pixel is illustrated in the fig. 2.6. The circuit is composed by a capacitor C, a p-MOS transistor, M_1 and by two n-MOS transistor, M_2 and M_3. The digital signal *Reset* and *RowSel*, row selection, control the gates of M_1 and M_3, while V_{DD} is the pixel supply voltage, [3].

In a photodiode hit by light, the passage of the current between anode and cathode proportional to the light intensity, is allowed The photodiode is

in parallel with the capacitor, which is the sum of the diode junction capacity and the input capacity of M_2 gate.

Before the exposure to the light, the Reset control, which sends in conduction the M_1 MOS, leads the capacitor at voltage V_{DD}, inversely biasing the photodiode. During the integration time, t_{int}, the photodiode, connected to a capacitor in parallel, permits the current I_{ph} to pass and then to discharges with the time the capacitor C, lowering the gate voltage of M_2 until to the value V_{lux}:

$$V_{lux} = V_{DD} - \frac{I_{ph}t}{C}. \tag{2.3}$$

The potential V_{lux} is transmitted to the M_2 source, which is an amplifier (source follower). When $RowSel$ is high, M_3, the signal passes to the analog to digital converter and it will be sent to the common line of the pixels of the same column. When the readout is ended M_3 returns low, M_1 becomes high, so that p-MOS is turned-off, and the new cycle begins [3].

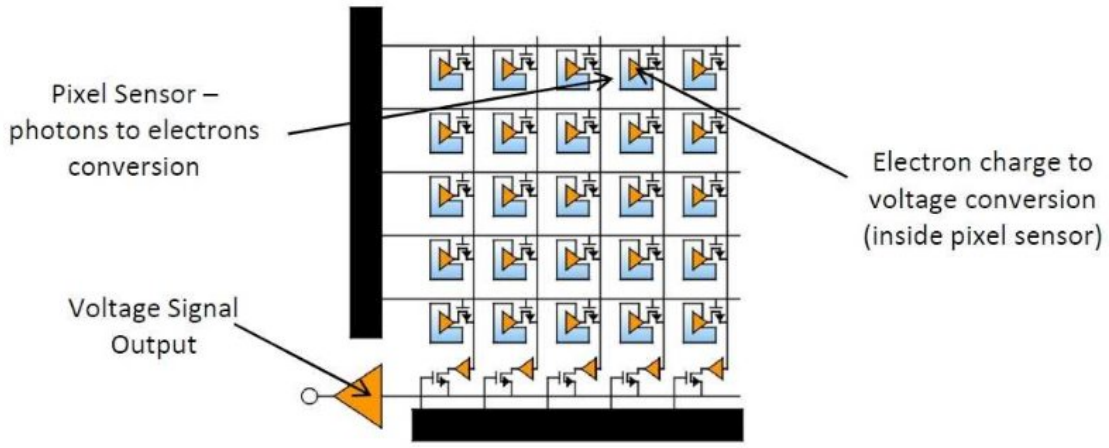

Figure 2.7: Array architecture, [20], [3].

A pixel array (fig. 2.7) is accessed one row at a time by enabling all the row-select transistors within the single row of pixels. At the bottom of the array, the individual pixels within the row are selected and read out column by column,[20].

For imaging applications, the signal from the photodiode is integrated and its accumulation provides a form of statistical binning that is a more faithful representation of light intensity that falls on the pixel.

A CMOS photosensor was chosen for our experiments, due to the accuracy in image acquisition, high resolution, and very low noise. The phtosensor will

be presented in the next chapter along with the triple-GEM device that was used for the measurements described in chapters 4 and 5.

Chapter 3

The GEMs optical readout

In this chapter, are described fundamentals of optical readout of a triple GEM detector and the device structure, together with the main optical parameter and the sensor are presented.

3.1 The origin

The aim of the experiment performed by Fraga et al [7] was the detection of thermal neutrons by a triple-GEM device filled with $^3HeCF_4$. The triple-GEM system had an optical readout obtained with a CCD camera equipped with a standard 50 mm f:1.8 photographic lens and cooled to -30°C.

Figure 3.1 shows the images of proton and tritium tracks recorded by Fraga et all [7] by means of a CCD looking at a triple GEM structure. The structure of the tracks is clearly seen in most events.

Figure 3.2 shows two images of tracks and the respective distributions of the scintillation light along the longitudinal CCD pixels of the track projection. The light variation along the tracks, due to the different energy deposition curves of the proton and the tritium,were identified, [7].

The results obtained by this study are an example on how it is possible to extract informations about the tracks of charged particles from the study of acquired images. The choice to perform a tracker based on a triple-GEM structure filled with a mixture that comprises CF_4 gas, derives by this and other studies. For optical readout, however, the use of a CMOS sensor has been chosen.

Figure 3.1: Images of proton and triton tracks obtained with HeCF_4 mixture, [7].

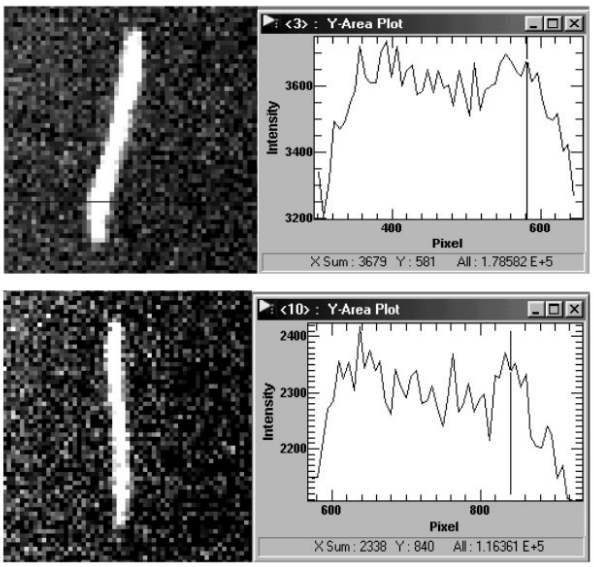

Figure 3.2: Distribution of measured scintillation along tracks. The Bragg curves of the proton (left) and tritium (right) are revealed, [7].

3.2 The ORANGE prototypes

The name ORANGE is the acronym for a particle tracker based on **o**ptically **rea**dout **GE**M . The light production associated to the electron multiplication, due to the passage of a charged particle through He/CF_4 gas mixture in the triple-GEM detector, allows to perform an optical read out. The passage of a charged particle through a He/CF_4 gas mixture in a Triple-GEM detector leads to light production associated to the electron multiplication, thus an optical read-out is possible. The big progress achieved in CMOS-based photosensors, even in commercial CMOS cameras, allows to obtain images with a very visible signals from minimum ionizing particles.

3.2.1 Triple-GEM based detectors

In this section we present the prototype layout associated to lab measurements.

The detector is composed by triple GEM structure, which was obtained by stacking three 10 $\times$10 cm^2 standard GEM foils. These foils are perforated with holes that have a bi-conical shape, whose diameter varies between 50 μm and 70 μm, as mentioned in chapter 1.

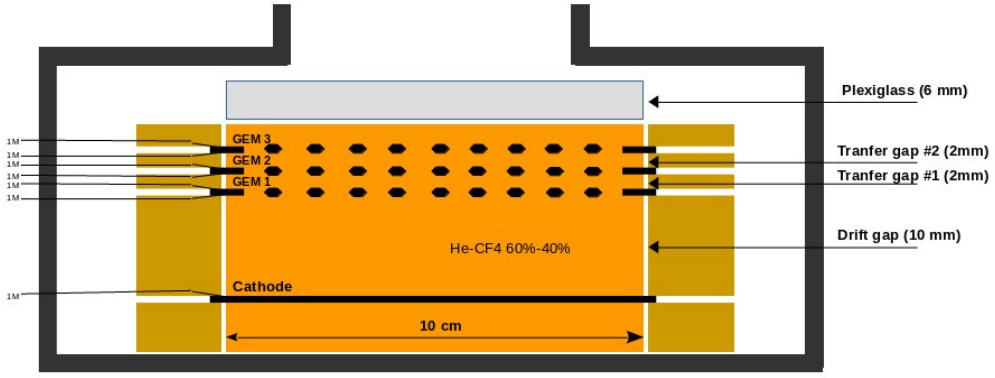

Figure 3.3: Drawing (not to scale) of the triple GEM stack of the second prototype.

In fig. 3.3, it is possible to see a section of the prototype system. The drift gap is the sensitive region of the device that occupies a volume larger than the other gaps; the ionization process takes place here where the primary electrons are produced. In our Triple-GEM device the drift volume is 10 mm, so the collection volume covers 100 cm^3. The first transfer gap is between

the first and the second GEM, while the second transfer gap is between the second and the third GEM; both gaps have a thickness of 2 mm. In these regions the clouds of electrons are carried through the three GEM foils.

Seven different high voltage channels are used to supply the detector electrodes through 1 $M\Omega$ protection resistors. The electrons created in the multiplication process induce a signal on the copper surface of the last GEM.

To allows the external readout of the light, the prototype have a transparent window made by a plexiglass tile, 6 mm thick, placed in front of the last GEM closing the gas volume.

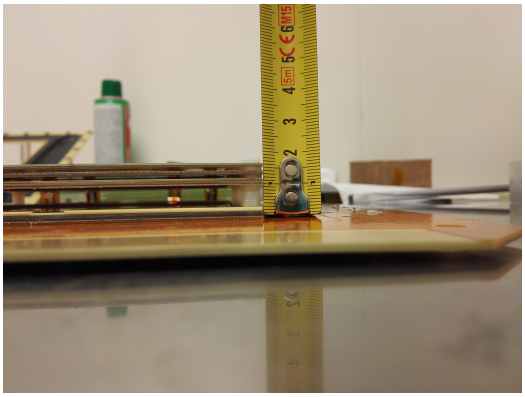

Figure 3.4: Picture taken during the detector assembling .

In fig. 3.4 it is possible to see a picture of the triple GEM stack assembled; the drift gap is clearly visible. Both the triple-GEM structures are placed in a black box, equipped with an upper window used for the image acquisition, which is placed right above the transparent cover.

3.3 Gas mixture

The gas mixture used in this device is composed by $HeCF_4$,whose percentages were chosen from the results obtained from previous studies [11]. The carbon tetra-fluoride CF_4 provides high electron drift velocities,it has low electron diffusion and it is a good and fast scintillator.

The optical emission spectrum of the CF_4 shows two peaks: the first in a range between 200 -350 nm and the second between 500-800 nm, see fig. 3.5.

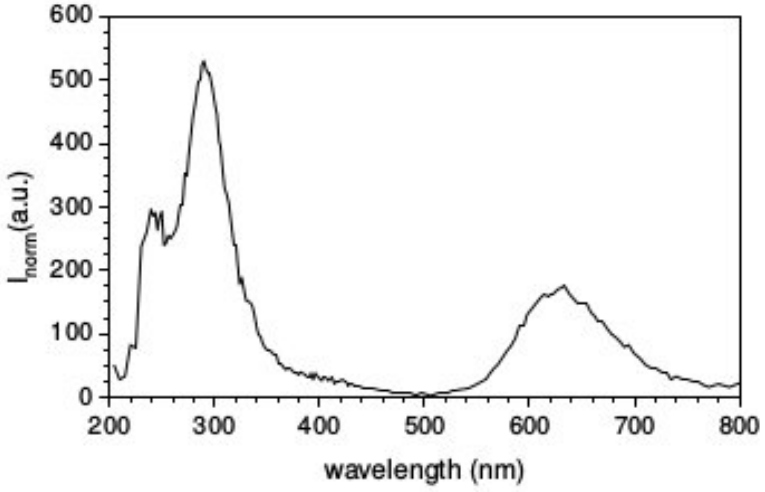

Figure 3.5: Light intensity, normalised to the current, as a function of the wavelength for $HeCF_4$ (60/40), [8].

The peaks in the visible region results from the excitation of a Rydberg state of CF_4 molecule that dissociates emitting CF_3 fragment; the threshold energy for this emission is 12.0 eV. The UV band seems to originate by CF_4^* ion that forms unstable molecular states and ionization processes, which are generally dissociative. One of the dissociation channels leads to the formation of an emitting CF_3^+ ion that could be responsible for the UV emission, [8].

3.4 The optical system

It is necessary to study the main equations which characterize the optical system. To understand and optimize the light emitted by the gas [10].

By using the thin lens approximation and simplifying the lens as a single converging lens, we can describe what happens when the light passes through the optical system.

A lens is a transmissive optical device that focuses or disperses a light beam through the refraction. The axis that pass through the physical center of the lens is the optical axis. With reference to fig. 3.6, we can see the lens indicated by L and its center , indicated by O. The object that emits the light is y that is at a distance s from the point O; the image of the object (y') is placed at a distance s' from the point O. The primary focus F is a point of the lens axis in which each ray, that comes from it or that is directed towards it, is propagated parallel to the axis due to the refraction. The secondary focus F' is a point of the lens axis in which each ray, that is

propagated parallel to the axis, is directed in it or appears to come from it, due to refraction. The distances of F and F' from lens are individuated by f and f', which are *focal distances*. In our case, the medium in which the light has been produced is the same in which the image is created, then, the refractive index does not change and this implies that $f = f'$.

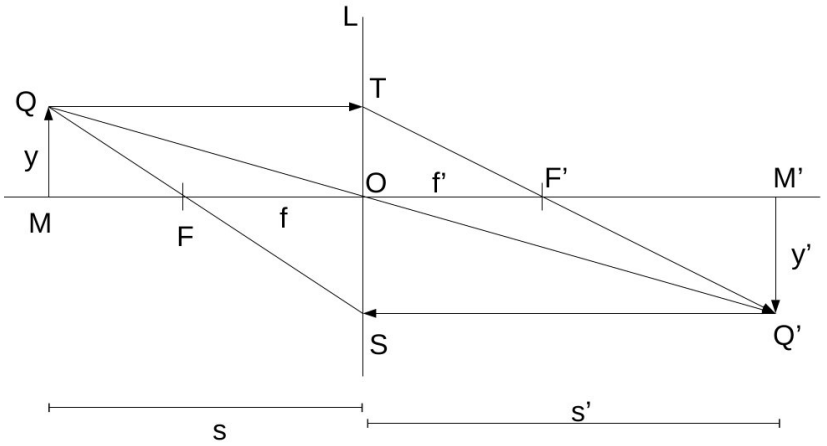

Figure 3.6: Schematic pictures on how an image is created by converging lens.

Because of the proportionality between the triangles $\widehat{Q'ST}$ and $\widehat{F'OT}$, and between $\widehat{QST}$ and $\widehat{FOS}$ it follows (fig. 3.6):

$$\frac{y - y'}{s'} = \frac{y}{f'} \qquad \frac{y - y'}{s} = \frac{-y'}{f} \tag{3.1}$$

which leads, with $f = f'$, to the conjugated points formula:

$$\frac{1}{s} + \frac{1}{s'} = \frac{1}{f} \tag{3.2}$$

Furthermore, by looking at triangles $\widehat{MOQ}$ and $\widehat{M'OQ}$:

$$\frac{s}{y} = \frac{s'}{y'} \qquad \frac{y'}{y} = \frac{s'}{s} \tag{3.3}$$

and also for triangles $\widehat{MFQ}$ and $\widehat{FOS}$, we can write the *magnification* I as:

$$I = \frac{s'}{s} = \frac{y'}{y} = \frac{f}{s - f} \tag{3.4}$$

The following cases are possible:

- $s < f \rightarrow$ virtual image;
- $f < s < 2f \rightarrow y' > y$ and $s' > s$: larger image;
- $s = 2f \rightarrow y' = y$ and $s' = s$: equal and equidistant image;
- s>2f $\rightarrow y' < y$ and $s' < s$: reduced image.

The magnification can be either described with another formula considering the other side of the lens, i.e. looking at the triangles $\widehat{TOF'}$ and $\widehat{F'M'Q'}$:

$$I = \frac{s'}{s} = \frac{y'}{y} = \frac{s' - f}{f} \tag{3.5}$$

Another important element to take in to account is the diaphragm of the lens: the amount of light that arrives to the sensor depends strongly on it. In the case of isotropic light emission, the photons reaching the sensor depend both on the distance and on the diaphragm of the lens. The lens aperture is defined as $\# = f/d$, where f is the focal length and d is the diaphragm diameter.

If the source is at a distance s, enough far from the lens so as to be considered point-like, the fraction of the photons that pass through the lens can be derived by

$$\Omega = \frac{\pi \left(\frac{d}{2}\right)^2}{4\pi \left(s\right)^2}, \tag{3.6}$$

which represents the geometrical acceptance.

Starting from the second magnification equation 3.5 we can find:

$$s' = (I + 1)f \tag{3.7}$$

and inserting it into the above equation:

$$\Omega = \frac{\pi \left(\frac{d}{2}\right)^2}{4\pi \left(s'\right)^2} = \left(\frac{d}{4\left(I + 1\right)f}\right)^2 \tag{3.8}$$

whence, remembering how the aperture of the diaphragm is defined we have:

$$\Omega = \frac{1}{\left(4(I + 1)\#\right)^2}. \tag{3.9}$$

which represents the fraction of the photons that reach the camera sensor.

3.5 The camera

In this work we use a ORCA-Flash 4.0 camera based on a CMOS image sensor and instrumented with a Schneider lens. The progresses that have been achieved in recent years for this type of sensors have led to the choice of this camera: speed in the acquisition and image sharpness, low noise, high sensitivity, are its characteristics. In fig. 3.7 we can see a picture of the camera equipped with its lens.

Figure 3.7: Picture of the camera.

The CMOS sensor is composed by 2048 × 2048 pixels with an area of 6.5 $\mu m \times$ 6.5 μm for a total sensitive surface of 13.3 mm × 13.3 mm providing, then, a high granularity (4 Mega Pixels).

The structure of the pixels consists of circuit that converts the incident light in electric signal by a photodiode and then into voltage within the pixel[1]. There is an on-chip column amplifier to achieve higher speed, allowing the simultaneous parallel readout of the signal. This allows low-noise and high-speed signal readout.

The element of CMOS image sensor is divided into upper and lower, each of which is placed with an on-chip column amplifier. This allows the simultaneous readout of two horizontal lines, achieving higher speed, fig. 3.8. The image readout starts from 2 central lines, the upper one of which moves toward the upper end and the lower one toward the lower end.

An important factor in determining the sensitivity is the efficiency in converting the light in to electric charge, or quantum efficiency. Since CMOS image sensor has multiple amplifiers arrayed in one pixel, the sensor unit that

[1]See Ref. [14].

performs the light-to-charge conversion is limited to a part of the pixel. Each pixel is equipped with an on-chip microlens, achieving increased sensitivity in comparison with the conventional CMOS image sensor. The sensibility of this device is about 70% for the visible wavelength range and, specifically, it reads the signal right that is around 600 nm (see fig. 3.9).

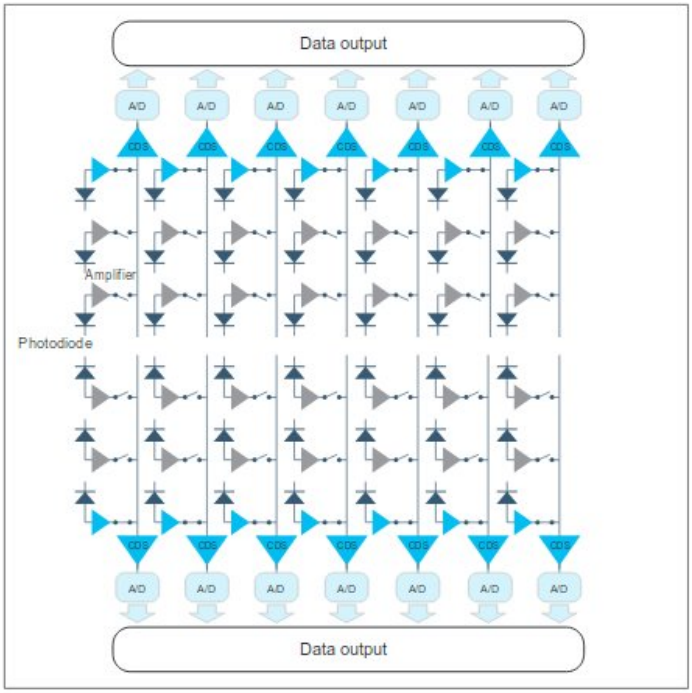

Figure 3.8: Readout circuit within CMOS image sensor, [14].

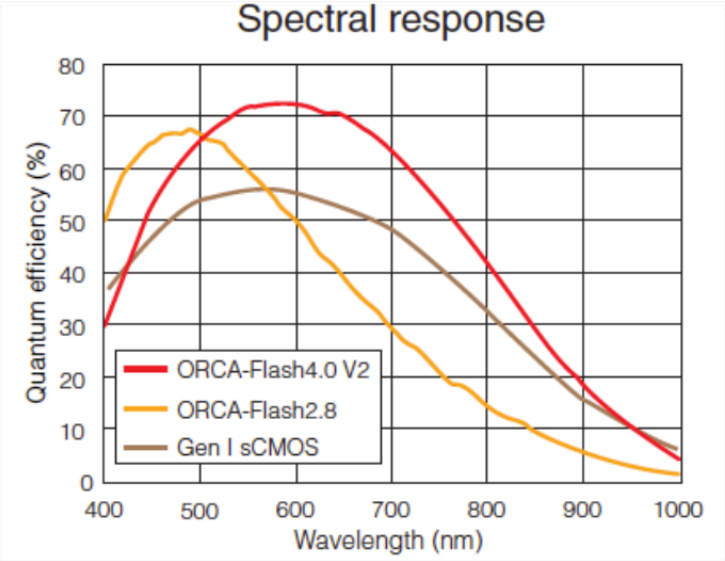

Figure 3.9: Spectral response, [14].

3.6 The Schneider lens

We used a Schneider Fast C-Mount Lens, adapted to reproduce the image of the track on the sensor of the camera. The lens has a focal length equal to 25 mm and a maximum aperture of f/0.95. This was required to collect the largest possible number of photons that come from sensitive area.

The optical system, then, was also equipped with a 1 mm ring spacer between the lens and the sensor which allowed to obtain the effective focal lens to about 20 mm. At a distance of about 20 cm:

- each pixel looks an area of 50 $\mu m \times$ 50 μm.
- the image of 10 $\times$ 10 cm^2 of the GEM can be acquired at a distance of 20 cm.

Chapter 4

Measurements with X-ray tube

In this chapter are presented results of tests performed with a photon beam, produced by an X-ray tube, impinging on a Fe target. Main task of these tests is to measure the detector electronic gain as a function of GEM high voltage supplied.

4.1 X-ray tube

An X-ray tube is a vacuum tube that converts electrical input into X-ray. The device consists in a cathode, which emits electron in vacuum, and an anode to collect them; thus an electric current in the tube is established. Electrons are accelerated across cathode and anode by means of an high voltage power source (generally between 10 and 150 kV). The X-ray spectrum depends on the anode material and the accelerating voltage.
Emitted from the cathode,electrons hit to the anode (usually made of tungsten, molybdenum or copper) and accelerate other electrons,ions and nuclei within the material. The X-ray are generated through bremsstrahlung process, and usually only 1% of the electron energy is converted in X-ray; the rest of the energy is released as heat.
To maximize bremsstrahlung X-ray output, it is desirable to use a target material with a high atomic number and therefore a nucleus with a larger positive charge; this characteristic makes electrostatic deflection of passing accelerated electrons more likely.

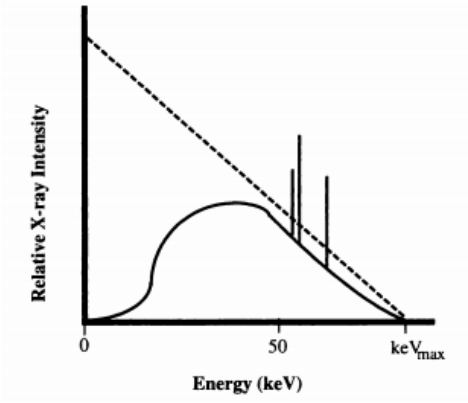

Figure 4.1: Emission spectrum for a tungsten target. The dotted line represents the unfiltered, bremsstrahiung portion of the X-ray spectrum emitted from the target. The solid line represents the total spectrum of X-rays after they have exited the X-ray tube and housing. The peaks in the solid line (vertical solid lines) are characteristic X-rays emitted by the X-ray tube. The total emission spectrum includes both bremsstrahbung and characteristic radiation.

The range of photonic energies emitted by the system can be adjusted by changing the applied voltage, and installing aluminum filters of varying thicknesses. Aluminum filters are installed in the path of the X-ray beam to remove non-penetrating radiation. The number of emitted X-ray photons, or dose, are adjusted by controlling the current flow and exposure time.

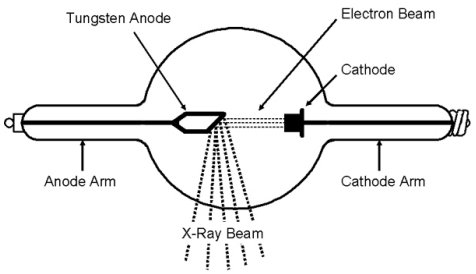

Figure 4.2: X-ray tube schematic

4.1.1 Components of X-ray tubes

The basic components of the X-ray tube include the cathode assembly, anode assembly, tube envelope, rotor and stator. (see next figure).

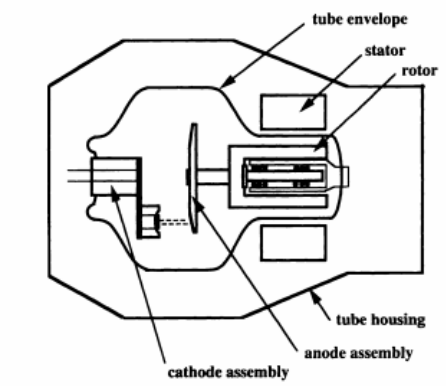

Figure 4.3: Diagram illustrates the basic components of the X-ray tube: the cathode assembly (electron source), the anode assembly, the tube envelope, the rotor and stator components of the electric induction motor (for rotating anodes only)

Cathode assembly

The cathode assembly is the source of electrons in the X-ray tube. A low-voltage circuit from the X-ray generator provides a current through the tube filament. The filament is made of tungsten and consists of a helical wire coil 10-20 mm in length and 2-5 mm in width within a focusing cup. The filament current emits electrons off the tungsten wire (thermionic emission). The high voltage between the cathode and anode creates an electric field.

Anode assembly

Two anode types are commonly used: fixed and rotating. Originally, a fixed anode was used, with tungsten target material imbedded in a fixed copper block. The low heat capacity of the fixed anode tube design limited its X-ray intensity. A substantial increase in X-ray intensity became possible with the development of a rotating anode (target) design. With a rotating anode, the instantaneous heat load produced at the focal point of the accelerated electrons.
The target material used in an X-ray anode, whether fixed or rotating, must have a high atomic number to maximize bremsstrahbung output. The target material must also tolerate a tremendous heat load.

X-ray tube envelope

The envelope is an important component of the X-ray tube because it maintains the required evacuated environment. If the internal tube elements

emit gas (outgas) or the vacuum fails, the tube becomes gassy and the gas molecules will impede electron flow between the cathode and anode. In this situation, the filament on the cathode is also likely to oxidize, causing the tube to fail.

Rotor and stator

The electric induction motor that turns the rotating anode consists of a rotor, which rotates on a set of bearings within the glass X-ray tube envelope, and the stator, which consists of wire windings external to the envelope. A variable magnetic field within the region of the rotor is induced by an alternating current applied to the stator. The metal rotor turns in response to the changing magnetic field, causing the attached anode to turn. Anode rotation speeds range from 3,000 rpm to 10,000 rpm for a high-speed anode. The stem is designed to protect the bearings from heat damage, a common cause of X-ray tube failure.

4.2 Measurements and data analysis

The experimental setup of test conducted in summer 2018 at LNF consists in a 20kV X-ray tube used as source, the ORANGE prototype, filled with an $HeCF_4$gas mixture, on 4 different proportions:(70/30;60/40;50/50;40/60). The number of electron hitting the iron target is function of the current I_T flowing in the filament; by changing the number of electrons on iron target, the number of photons produced by bremsstrahlung changes. To evaluate the behaviour of the X-ray tube and set a I_t suitable for the experiment, the trend of current collected on the third GEM vs I_t has been studied.
A linear trend appeared only for first three point, with $I_t < 110\ \mu A$, thus I_t was considered a fixed parameter and set on $I_t = 0.1mA$ throughout the data taking sessions.The divergence between the two trends is due to space charge effect: as I_t rises a linear response is expected for the current collected on third GEM; although, when the charge amount in the GEM holes is too high, the external electric field tends to be shielded and the electric field gets lower and the gain is no longer stable.

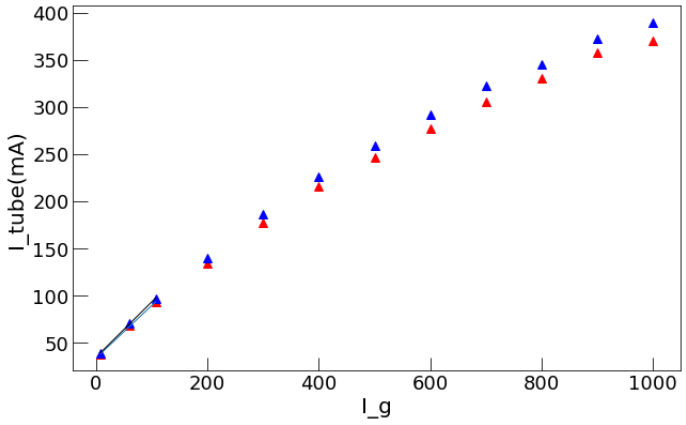

Figure 4.4: Space charge effect: the gain is no longer stable, inducing a non linear trend

The X-rays produced with the tube hit on the gas mixture and ionizes atoms and molecules extracting primary electrons; these electrons are multiplied by the avalanche processes through the triple-GEM and are collected on the third GEM where the corresponding current is read by electronics.
The flux of photon produced in the gas is:

$$\phi_\gamma = \frac{N_\gamma}{\Delta t} \tag{4.1}$$

and is proportional to the flux of primary electron.
The number of secondary electrons collected on the third GEM give rise to the current I_{G3D} that is:

$$I_{G3D} = \phi_{ep} \cdot G = \phi_\gamma \cdot K \cdot G = I_t \cdot \alpha \cdot K \cdot G \tag{4.2}$$

where ϕ_{ep} is the flux of primary electrons produced by X-ray in the gas; G is the gain; ϕ_γ is the photons flux in the gas; K and α are constant taking into account the photoelectric cross-section in a particular gas.
Since I_t was a fixed parameter; α and k are constant, we can write:

$$I_{G3D} = \beta G \tag{4.3}$$

Gain is a function of the gas mixture and the HV supplied to the detector. For every gas mixture used in the test we can write G as:

$$G(gas) = Ae^{\delta V_{gem}} \tag{4.4}$$

The values of I_{G3D} as a function of V_{GEM} have been studied for the gas mixtures:

$V_{GEM}(V)$	$I_{G3D}(nA)$
365	78
370	91
375	106
380	121
385	140
390	160
395	182
400	205
405	230
410	260

Table 4.1: Current on third GEM for 70/30 mix

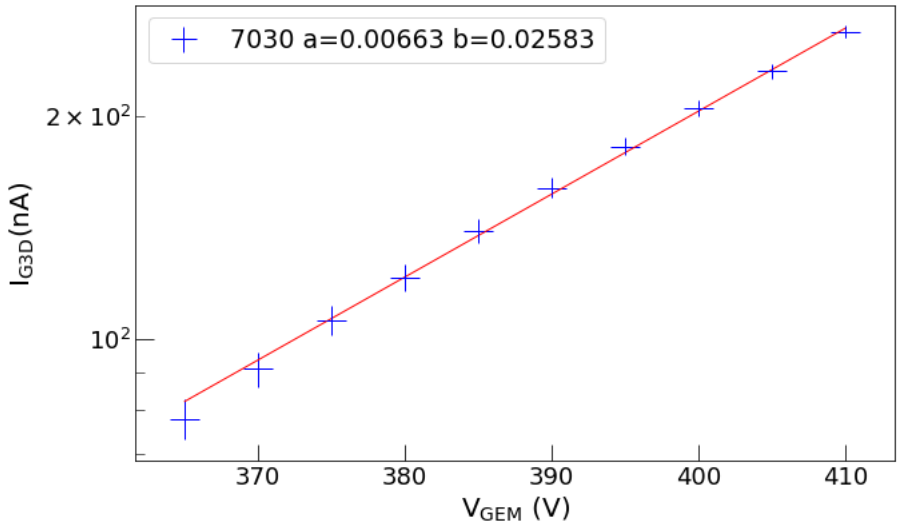

Figure 4.5: Current on third GEM for 70/30 mix as a function of V_{GEM}

$V_{GEM}(V)$	$I_{G3D}(nA)$
400	96
405	111
410	130
415	144
420	164
425	182
430	207
435	230
440	255

Table 4.2: Current on third GEM for 60/40 mix as a function of V_{GEM}

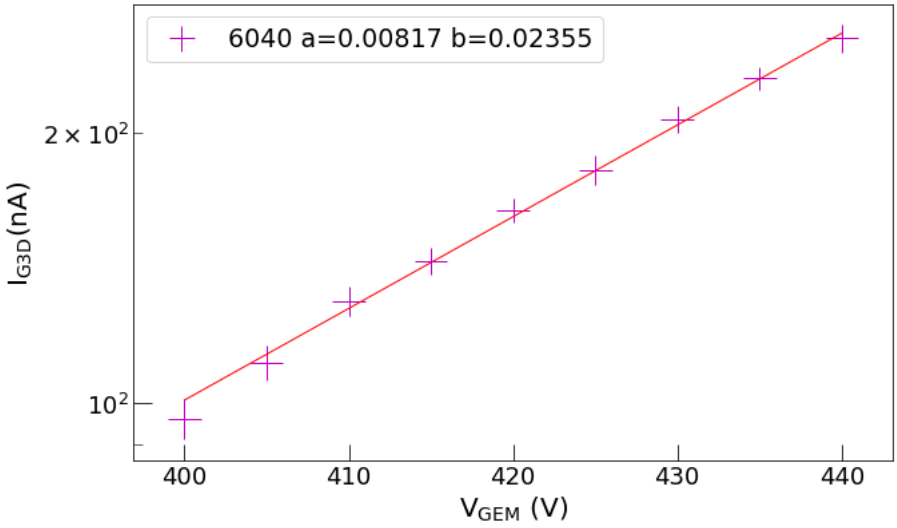

Figure 4.6: Current on third GEM for 60/40mix

$V_{GEM}(V)$	$I_{G3D}(nA)$
400	36
405	43
410	52
415	62
420	73
425	85
430	102
435	117
440	133
445	150
450	169
455	183
460	205

Table 4.3: Current on third GEM for 50/50 mix as a function of V_{GEM}

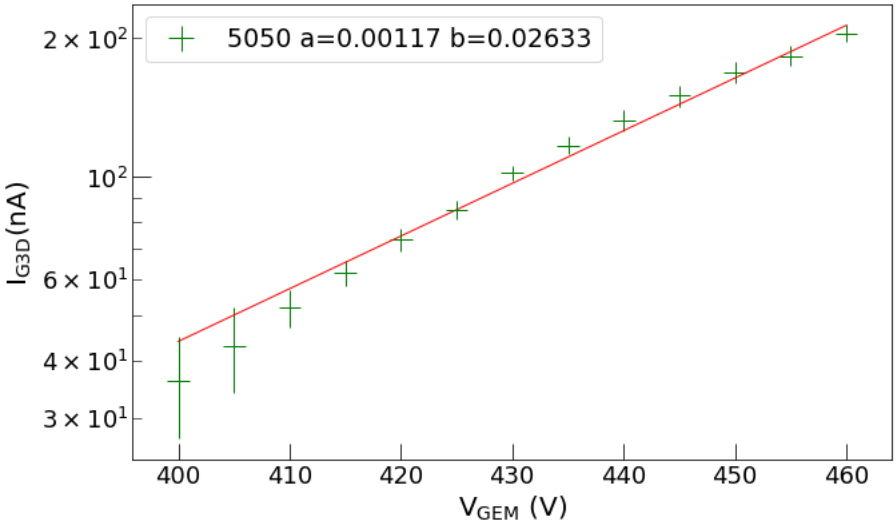

Figure 4.7: Current on third GEM for 50/50mix

$V_{GEM}(V)$	$I_{G3D}(nA)$
420	19
425	24
430	29
435	36
440	45
445	55
450	66
455	78
460	94

Table 4.4: Current on third GEM for 40/60 mix as a function of V_{GEM}

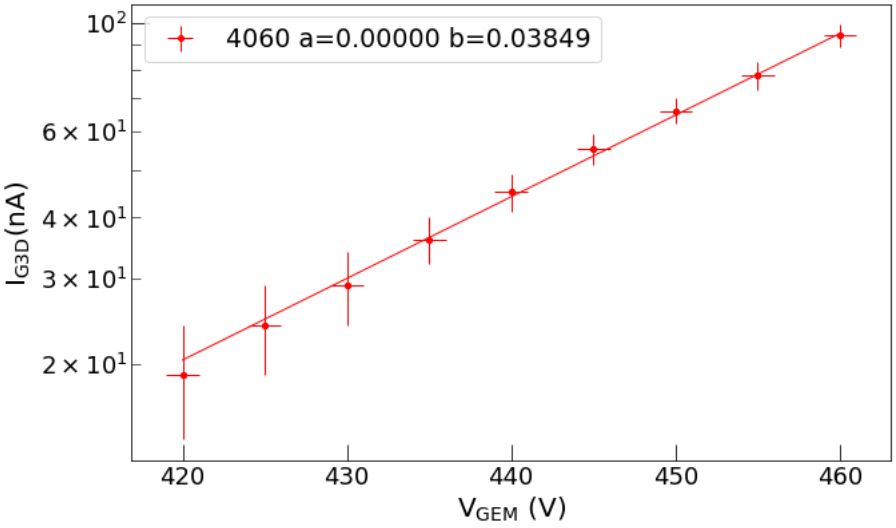

Figure 4.8: Current on third GEM for 40/60mix

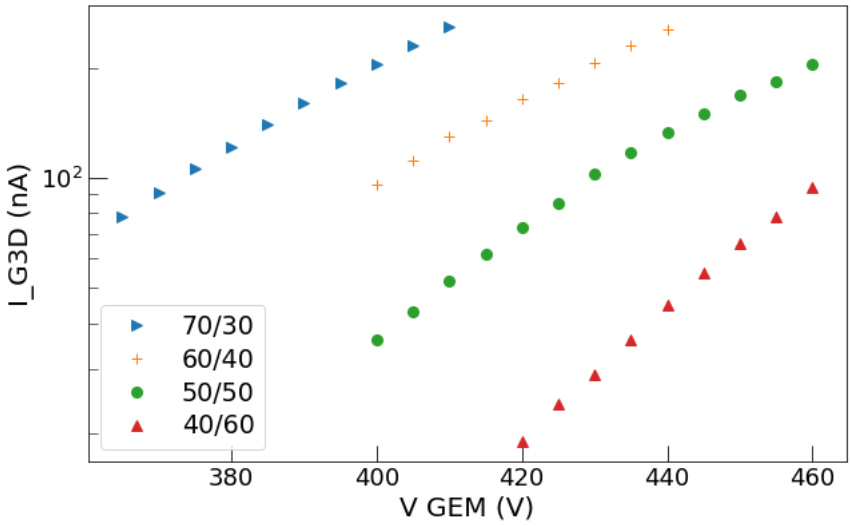

Figure 4.9: Current on third GEM for all mixtures as a function of V_{GEM}

For every gas mixture the values of A and δ have been extracted from exponential fit on the I_{G3D} vs V_{GEM} plot:

	A(nA)	$\delta(nA/V)$
70/30	$6.62 \cdot 10^{-3}$	0.026
60/40	$8.17 \cdot 10^{-3}$	0.023
50/50	$1.17 \cdot 10^{-3}$	0.026
40/60	$1.94 \cdot 10^{-6}$	0.038

Table 4.5: A and δ values from exponential fit

The gain for every gas mixture had been computed taking into account previous experiments [6]: another detector with the same structure and same parameter ($I_t = 100mV$ and 20 kV), with gain of $G : 1.24 \cdot 10^6$ produced a current of 360 nA.
So we can compute our gain as:

$$G(gas) = 1.24 \cdot 10^6 \cdot \frac{I_{G3D}}{360nA} \tag{4.5}$$

For every gas mixture the gain values are:

$V_{GEM}(V)$	Gain
365	$2.69 \cdot 10^5$
370	$3.13 \cdot 10^5$
375	$3.65 \cdot 10^5$
380	$4.17 \cdot 10^5$
385	$4.82 \cdot 10^5$
390	$5.51 \cdot 10^5$
395	$6.27 \cdot 10^5$
400	$7.06 \cdot 10^5$
405	$7.92 \cdot 10^5$
410	$8.96 \cdot 10^5$

Table 4.6: Gain values for 70-30 mix

$V_{GEM}(V)$	Gain
400	$3,31 \cdot 10^5$
405	$3,82 \cdot 10^5$
410	$4,48 \cdot 10^5$
415	$4.96 \cdot 10^5$
420	$5.65 \cdot 10^5$
425	$6.27 \cdot 10^5$
430	$7.13 \cdot 10^5$
435	$7.92 \cdot 10^5$
440	$8.78 \cdot 10^5$

Table 4.7: Gain values for 60-40 mix

$V_{GEM}(V)$	Gain
430	$3.51 \cdot 10^5$
435	$4.03 \cdot 10^5$
440	$4.58 \cdot 10^5$
445	$5.17 \cdot 10^5$
450	$5.82 \cdot 10^5$
455	$6.30 \cdot 10^5$
460	$7.06 \cdot 10^5$

Table 4.8: Gain value for 50-50 mix

$V_{GEM}(V)$	Gain
420	$6.54 \cdot 10^4$
425	$8.27 \cdot 10^4$
430	$9.99 \cdot 10^4$
435	$1.24 \cdot 10^5$
440	$1.55 \cdot 10^5$
445	$1.89 \cdot 10^5$
450	$2.27 \cdot 10^5$
455	$2.69 \cdot 10^5$
460	$3.24 \cdot 10^5$

Table 4.9: Gain value for 40-60 mix

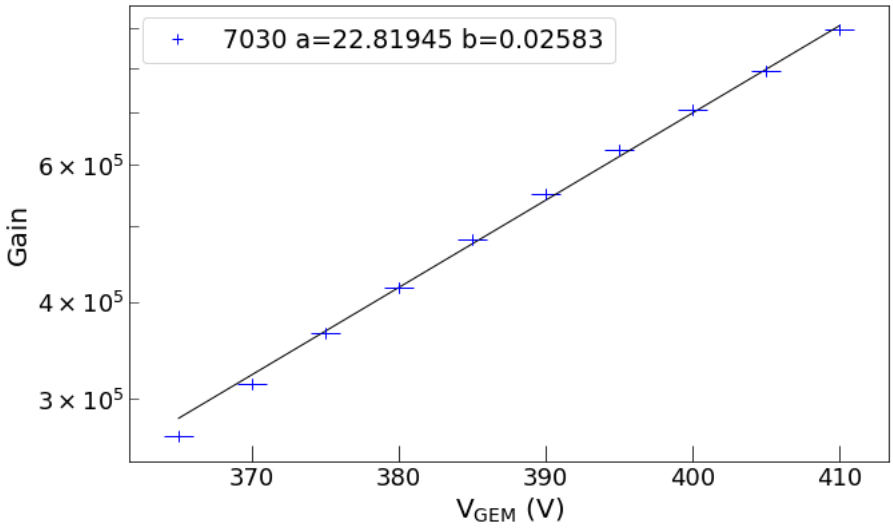

Figure 4.10: Gain values for 70/30 mix as a function of V_{GEM}

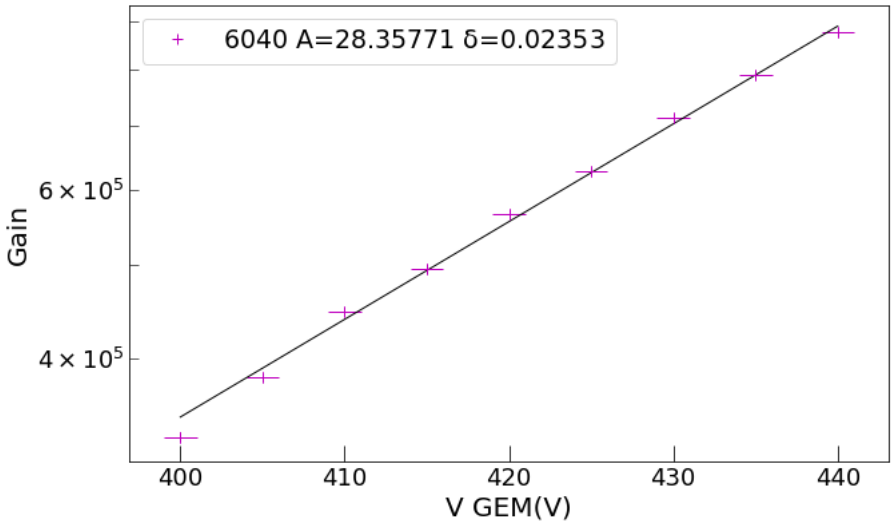

Figure 4.11: Gain values for 60/40 mix as a function of V_{GEM}

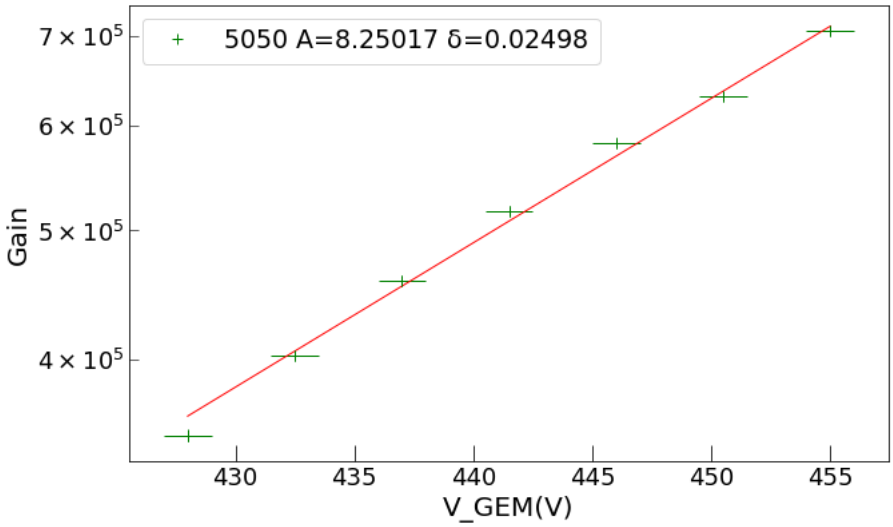

Figure 4.12: Gain values for 50/50 mix as a function of V_{GEM}

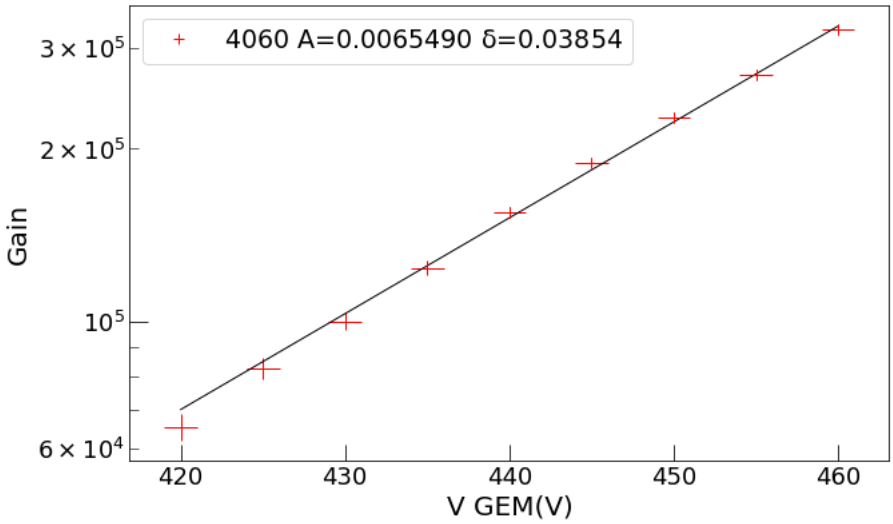

Figure 4.13: Gain values for 40/60 mix as a function of V_{GEM}

The exponential fit on the Gain vs V_{GEM} plot returns the intercept and angular coefficient for every gas mix:

	A	$\delta(V^{-1})$
70/30	22.82	0.026
60/40	28.36	0.023
50/50	8.25	0.026
40/60	$6.55 \cdot 10^{-3}$	0.038

Table 4.10: A and δ values from exponential fit

The A and δ values are useful to extrapolate the gain at 400 V for the missing point in the data sets.

	A	$\delta(V^{-1})$	Gain(400V)
70/30	22.82	0.026	$7.06 \cdot 10^5$
60/40	28.36	0.023	$3,31 \cdot 10^5$
50/50	8.25	0.026	$1.85 \cdot 10^5$
40/60	$6.55 \cdot 10^{-3}$	0.038	$3.24 \cdot 10^4$

Table 4.11: A and δ values from exponential fit

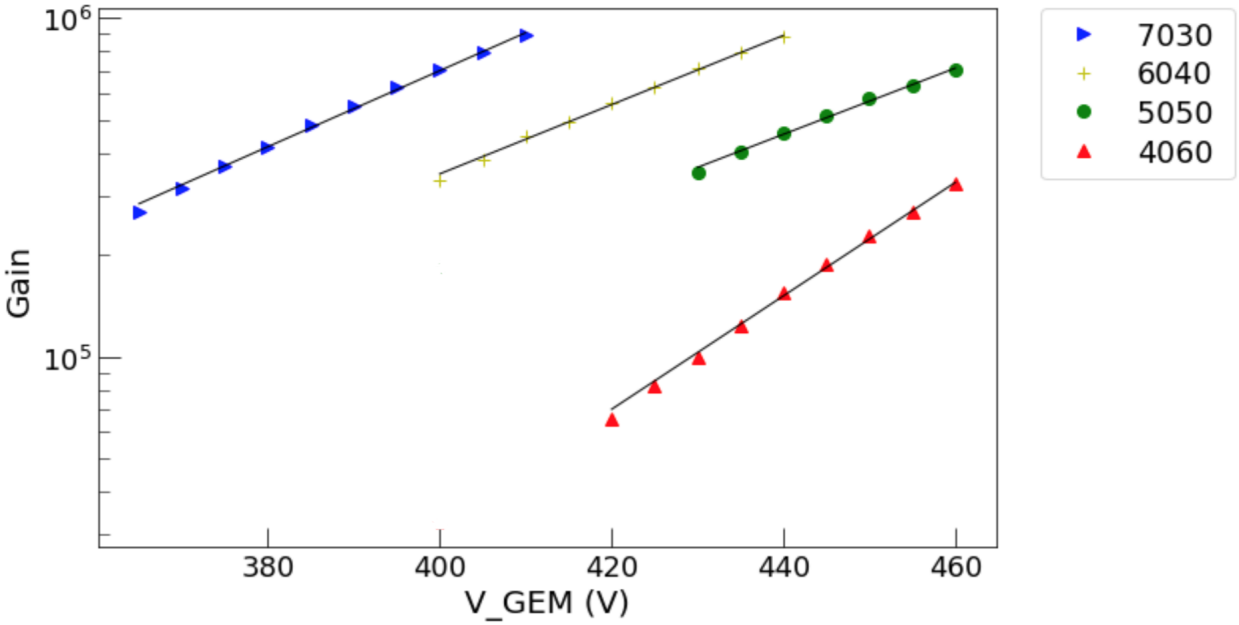

Figure 4.14: Gain for all mixtures combined plot

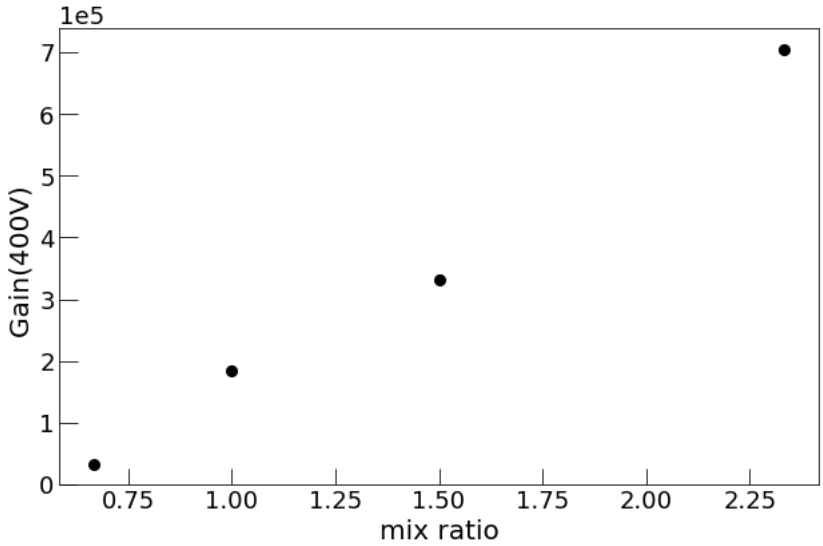

Figure 4.15: Gain as a function of mix ratio plot

Chapter 5

Measurements with CMOS

This chapter presents the results of various data taking sessions performed at Frascati National Laboratories[13], with the ORANGE prototype and CMOS. The data were analyzed through simple algorithms .

5.1 Experimental setup

For this session of acquisition it was used ^{55}Fe as x-ray source. ^{55}Fe decays via electron capture to ^{55}Mn with a half-life of 2.737 years [5]. The electrons around the nucleus rapidly adjust themselves to the lowered charge without leaving their shell, and shortly thereafter the vacancy in the "K" shell left by the nuclear-captured electron is filled by an electron from a higher shell. The difference in energy is released by emitting Auger electrons of 5.19 keV, with a probability of about 60%, K-α-1 X-rays with energy of 5.8987 keV and a probability about 16.2%, K-α-2 X-rays with energy of 5.8876 keV and a probability of about 8.2%. The energies of the K-α-1 and -2 X-rays are so similar that they are often specified as mono-energetic radiation with 5.9 keV photon energy. Its probability is about 28% [9].
The ORANGE prototype as filled with a $HeCF_4$ mixture in five different percentages: (80/20; 70/30;60/40;50/50;40/60)%. The gas in the detector was set on atmospheric pressure, and the gas flow controlled by a fluxmeter. The drift field was set 1 kV/cm while the transfer field 2 kV/cm.
For every gas mixture, different acquisitions have been performed and light produced by ionization in gas has been collected as a function of high voltage supplied to the triple-GEM detector.
Light has been read-out via ORCA-Flash 4.0 camera based on a CMOS sensor. The camera was connected to the ORANGE prototype and covered with a black optical cloth to reduce external light.

Figure 5.1: The ORANGE prototype connected to camera

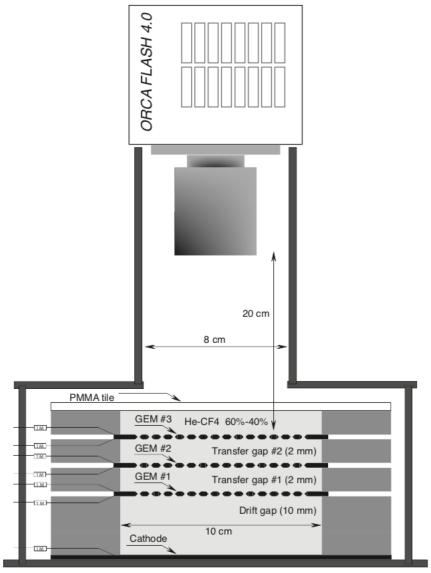

Figure 5.2: Drawing (not to scale) of the ORANGE prototype stack with lens and the CMOS camera

5.2 Escape peak

The main interaction expected in the detector is the interaction between ^{55}Fe x-ray and gas molecules, with an energy release of 5.9 keV.
In the photoelectric absorption, the incident photon disappears and a photoelectron is produced from one of the electron shells of the absorber. The

kinetic energy that this electron carries off is $Ee^- = h\nu - E_b$, where E_b is the binding energy of the liberated electron in its original shell. This empty spot in the electron shell is quickly filled by electron rearrangement.This process causes the binding energy, E_b, to be liberated as well. This energy is liberated in the form of a characteristic X-ray or an Auger electron.

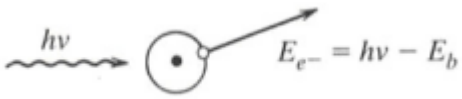

Figure 5.3: A depiction of photoelectric absorption

When characteristic X-ray is released by an absorber atom, it is in most cases reabsorbed near the atom that emitted it. If this process takes place near the surface of a detector, the characteristic X-ray may escape the detector and alter the response function as Figure 5.3 shows:

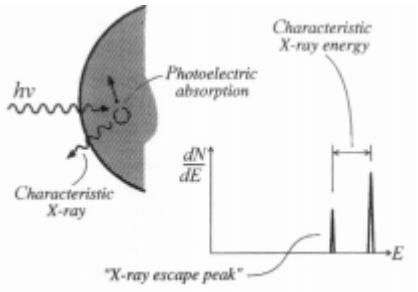

Figure 5.4: A characteristic X-ray escaping a detector and the effect it has on the response function.

By escaping, the characteristic X-ray creates a new peak in the response function. This peak appears a distance of the characteristic X-ray energy away from the photopeak and is known as the X-ray escape peak. This phenomena is prevalent in low energy incident photons and detectors with a large surface-to-volume ratio. The escape peak has a mean pulse height proportional to the difference between the photon energy of the incident X-rays and of the spectral characteristic line of the detector gas.

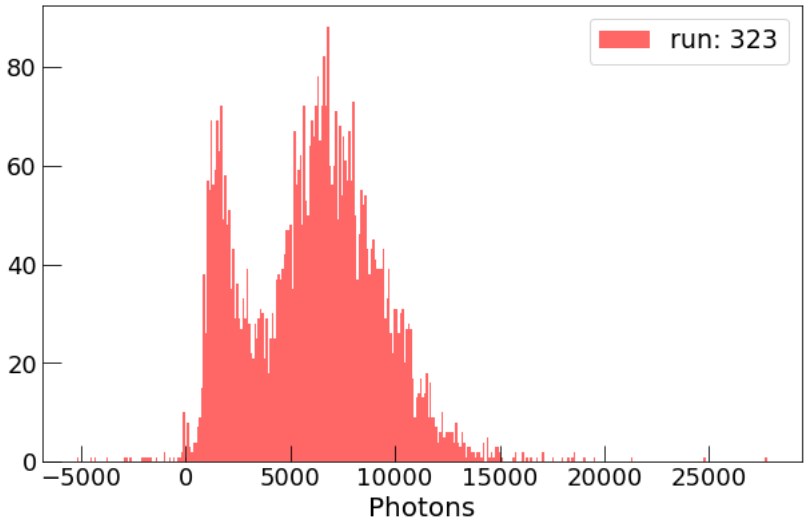

Figure 5.5: histogram with pedestal at 0, escape peak and main peak

The size of the escape peak is a function of fluorescent yield,ω and is generally smaller than the characteristic peak because relatively few X-rays excite the gas compared with the number detected; however, in some cases its size can be quite large.

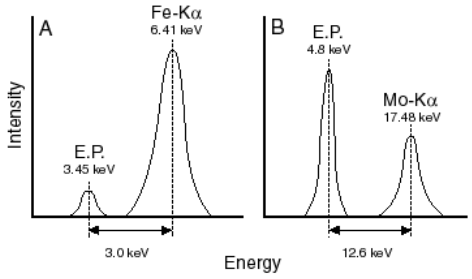

Figure 5.6: Escape peak: (A) In argon ($\omega = 0.12$); (B) in krypton ($\omega = 0.65$)

5.3 Data taking

For every gas mixture an high voltage scan to study the photoemission in the gas. It was chosen an exposition time for the camera of 0.3 second, and a number of acquisition of 600. The maximum high voltage supplied to the GEMs was set to avoid overcurrent in detector and the resulting breaking of the apparatus.
For every acquisition has been produced a (2048×2048 pixels image) containing track of the photoemission by the gas molecules. The tracks have a

circular shape due to the low energy γ emitted by the ^{55}Fe and its Compton interaction with gas molecules. The total distribution of the circular tracks center can be seen in the next figures.

To analyze the images, an algorithm based on the Circle Hough transform [17] has been used.

5.4 The Hough transform

The Hough transform is a feature extraction technique used in image analysis, computer vision, and digital image processing. The purpose of the technique is to find imperfect instances of objects within a certain class of shapes by a voting procedure. This voting procedure is carried out in a parameter space, from which object candidates are obtained as local maxima in a so-called accumulator space that is explicitly constructed by the algorithm for computing the Hough transform.

In automated analysis of digital images, a subproblem often arises of detecting simple shapes, such as straight lines, circles or ellipses. In many cases an edge detector can be used as a pre-processing stage to obtain image points or image pixels that are on the desired curve in the image space. Due to imperfections in either the image data or the edge detector, however, there may be missing points or pixels on the desired curves as well as spatial deviations between the ideal line/circle/ellipse and the noisy edge points as they are obtained from the edge detector. For these reasons, it is often non-trivial to group the extracted edge features to an appropriate set of lines, circles or ellipses. The purpose of the Hough transform is to address this problem by making it possible to perform groupings of edge points into object candidates by performing an explicit voting procedure over a set of parameterized image objects (Shapiro and Stockman, 304).

The simplest case of Hough transform is detecting straight lines. In general, the straight line y = mx + b can be represented as a point (b, m) in the parameter space. However, vertical lines pose a problem. They would give rise to unbounded values of the slope parameter m. Thus, for computational reasons, Duda and Hart[5] proposed the use of the Hesse normal form:$r = x\cos\theta + y\sin\theta$

where r is the distance from the origin to the closest point on the straight line, and θ is the angle between the x axis and the line connecting the origin with that closest point.

It is therefore possible to associate with each line of the image a pair (r, θ). The (r, θ) plane is sometimes referred to as Hough space for the set of

straight lines in two dimensions.

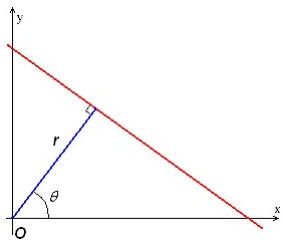

Figure 5.7: r,θ line parametrization in the simplest case of Hough transform

Given a single point in the plane, then the set of all straight lines going through that point corresponds to a sinusoidal curve in the (r, θ) plane, which is unique to that point. A set of two or more points that form a straight line will produce sinusoids which cross at the (r, θ) for that line. Thus, the problem of detecting collinear points can be converted to the problem of finding concurrent curves.

The linear Hough transform algorithm uses a two-dimensional array, called an accumulator, to detect the existence of a line described by $r = x \cos\theta + y \sin\theta$. The dimension of the accumulator equals the number of unknown parameters, i.e., two, considering quantized values of r and θ in the pair (r, θ). For each pixel at (x,y) and its neighborhood, the Hough transform algorithm determines if there is enough evidence of a straight line at that pixel. If so, it will calculate the parameters (r, θ) of that line, and then look for the accumulator's bin that the parameters fall into, and increment the value of that bin. By finding the bins with the highest values, typically by looking for local maxima in the accumulator space, the most likely lines can be extracted, and their (approximate) geometric definitions read off. The simplest way of finding these peaks is by applying some form of threshold, but other techniques may yield better results in different circumstances – determining which lines are found as well as how many. Since the lines returned do not contain any length information, it is often necessary, in the next step, to find which parts of the image match up with which lines. Moreover, due to imperfection errors in the edge detection step, there will usually be errors in the accumulator space, which may make it non-trivial to find the appropriate peaks, and thus the appropriate lines.

The final result of the linear Hough transform is a two-dimensional array similar to the accumulator—one dimension of this matrix is the quantized angle θ and the other dimension is the quantized distance r. Each element of the matrix has a value equal to the sum of the points or pixels that are positioned on the line represented by quantized parameters (r, θ). So

the element with the highest value indicates the straight line that is most represented in the input image.

In our analysis was used the algorithm for detecting circular object instead of straight lines, the circle Hough Transform (CHT).
The algorithm is based on the following steps:

- First, the accumulator space, which is made up of a cell for each pixel, is created Initially each cell is set to 0.
- For each edge point (i, j) in the image, increment all cells which according to the equation of a circle $(i-a)^2+(j-b)^2=r^2$ could be the center of a circle. These cells are represented by the letter a a in the equation.
- For each possible value of a a found in the previous step, find all possible values of b which satisfy the equation.
- Search for local maxima in the accumulator space. These cells represent circles that were detected by the algorithm.

5.5 Data analysis

In our algorithm the complete image was scaled by a factor of 4 and rebined to identify edges more clearly.

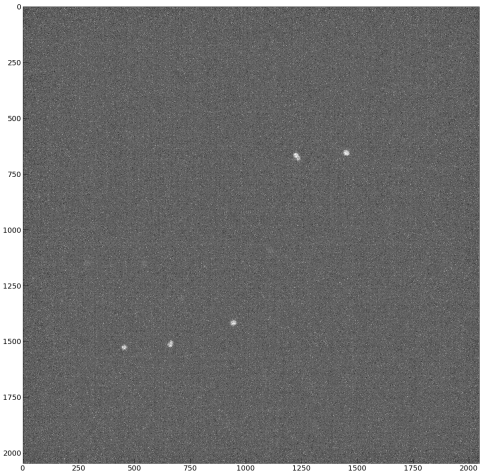

Figure 5.8: Original image acquired by the CMOS sensor based camera

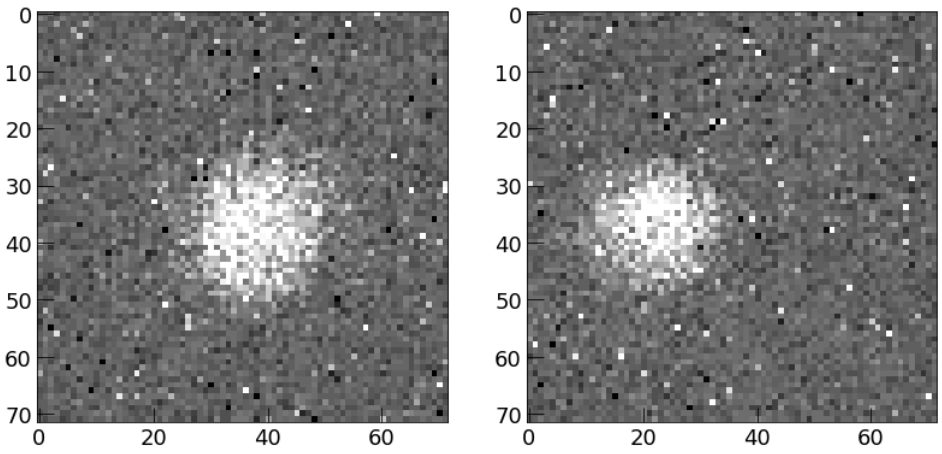

Figure 5.9: Rescaled images of two tracks acquired by CMOS sensor based camera

A threshold on pixel content was set, to identify the edges of the circles, taking into account only the pixel with a light content between 101 and 150. The circles identification in the digital image is a stochastic process, so it was necessary to set a range of possible radius to detect; it was chosen an interval between 1 and 4, to scan with a step of 0.1 and a maximum number of circles, in our case set to 20.

```
scale=(dataImage.shape[1]/rescale)
imgRes = my.rebin(dataImage, (rescale, rescale))
edges = (imgRes>101) & (imgRes<150) #pixel content threshold
hough_radii = np.arange(1, 4, 0.1)  #possible radii interval
hough_res = hough_circle(edges, hough_radii)

accums, cxh, cyh, radii = hough_circle_peaks(hough_res, hough_radii,
                                             total_num_peaks=20)        #hough transform
```

Figure 5.10: Example of Hough transform script: the image rescaling, threshold setting, and radii interval are shown

Once the circles have been found, it was necessary to delete the doubles; among all possible circles, if the distance on the two axis between the circles is smaller than the radius returned from the Hough function, the circles are deleted, saving only one.

```
while i < len(cxh):
    j=0
    while j < len(cxh):
        if len(cxh)>i:

            if abs((cxh[i]-cxh[j]))+abs((cyh[i]-cyh[j])) < radii[j] and i!=j :

                cxh = np.delete(cxh, j)
                cyh = np.delete(cyh, j)
                radii = np.delete(radii, j)
                j-=1
        j+=1
    i+=1
```

Figure 5.11: Doubles deleting script: the circles found at distance smaller than radii are deleted

For the gas mixtures 70-30 at 400 V, most probable radius was found to be about 8 pixels. We know [14] the scale for pixels is $50\mu m$ per pixels,hence the tracks deriving from interaction between photons and the gas mixtures have an actual radius of $400\mu m$

In the next figure is shown the identification of the tracks.

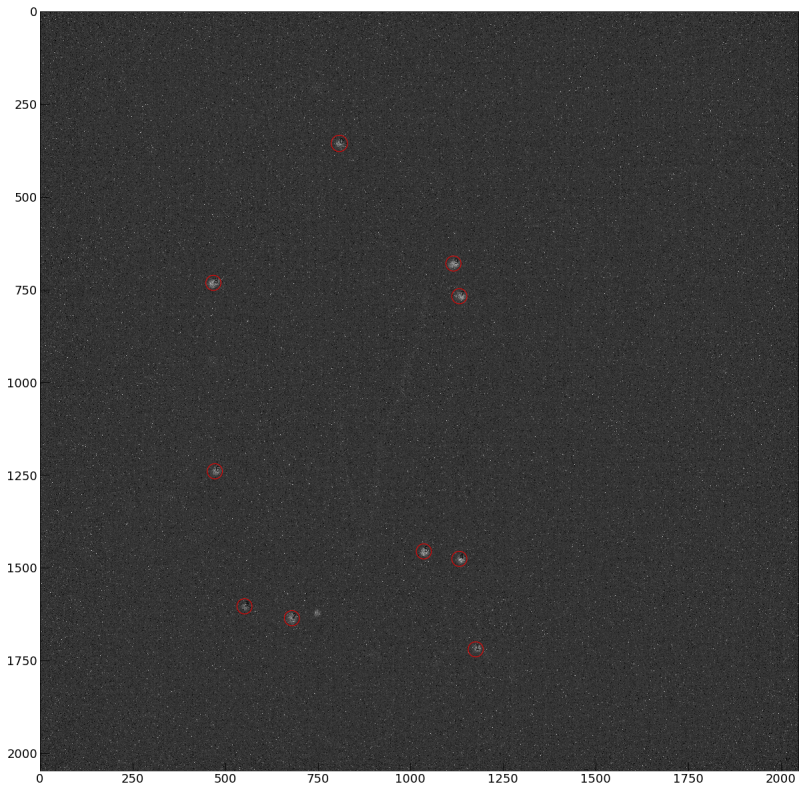

Figure 5.12: Screen showing the identified circles tracks

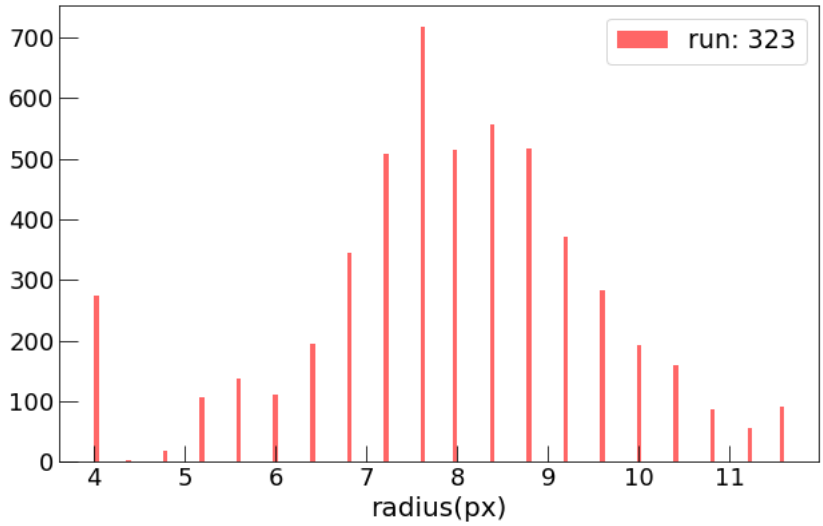

Figure 5.13: Histogram of the tracks radii distribution. The most frequent radius is about 8 pixel

The intensity plot of the circles as a function of distance from the source presents a trend that is compatible with the expected results; taking into account detector geometric acceptance, it is shown that most if interactions occurs in the area close to the source.

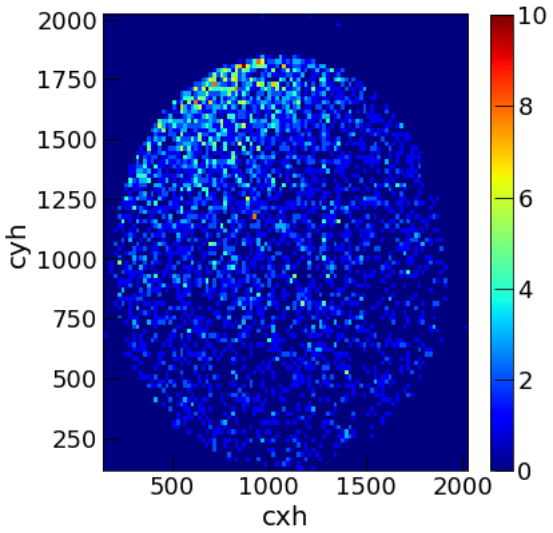

Figure 5.14: Intensity plot of the circles distribution. Most of interaction occurs in the region close to the source (placed around (750;2000) coordinates)

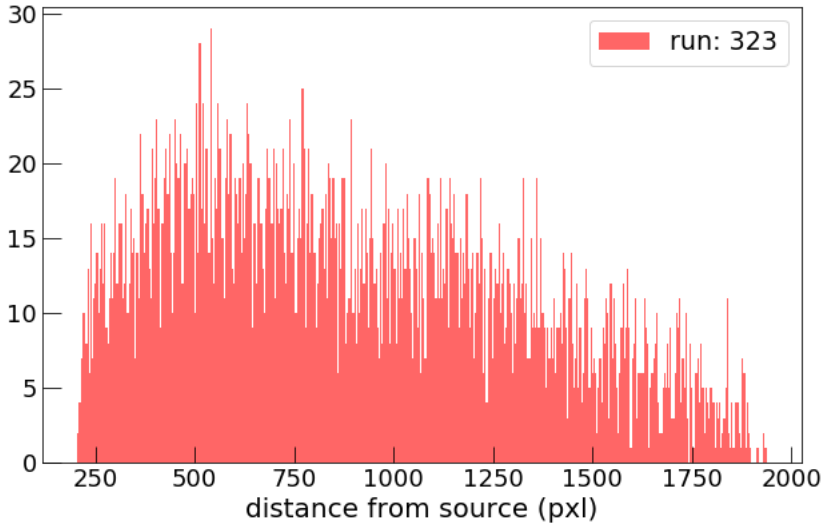

Figure 5.15: Histogram of distances from source

5.5.1 Persistence and background rejection

It is possible that in some images a phenomenon called "persistence" occurs, it is due to slow rate at which the pixel in the detector are emptied.The main hardware cause of the persistence in the detctor has to be searched at dyodes level in the depletion zone. It is habit to think that in a dyodes the signal is created only in the depletion zone where the free charges sense the electric field and move towards the electrode. However outside the depletion zone where there is no electric field, charges move for diffusion, and on larger scale of time the charge produced outside the depletion zone can reach the electrode and create a signal. Thus, a large part of the signal is collected and read very fast, when the light is emitted, and another share of the signal is collected on a larger scale of time. Thus,it is possible that the second part of the signal is read even if the first part is not completely collected, giving rise to the persistence, see Figure 5.16

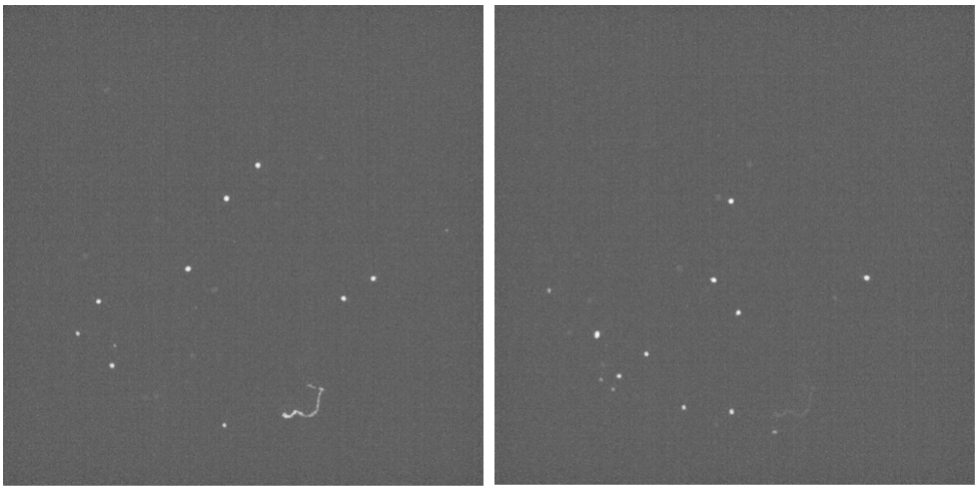

Figure 5.16: Track persistence: image n-1 (left) and image n (right). In the right image less intens tracks in the same spots are visible

To exclude the persistence effect, in the analysis from every images has been subtracted the sum of the light of two previous images. This procedure also implies the background subtraction.

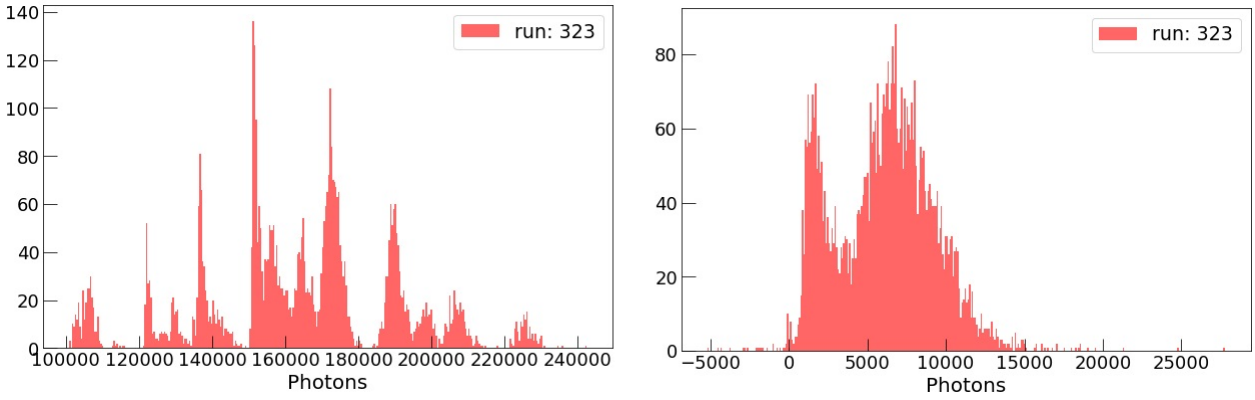

Figure 5.17: Histogram of signal+backgrond(left); background subtracted (right)

5.5.2 Data fitting

For every gas mixture a voltage scan has been performed collecting the light and the resulting plots have been fit with a Polya function to evaluate the mean number of photons for every run, hence the light intensity.

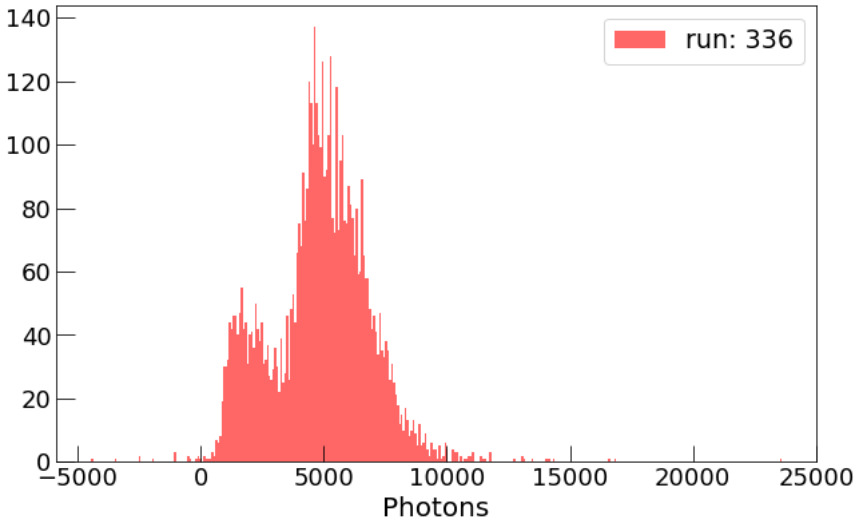

Figure 5.18: Photons distribution for 70/30 gas mixture

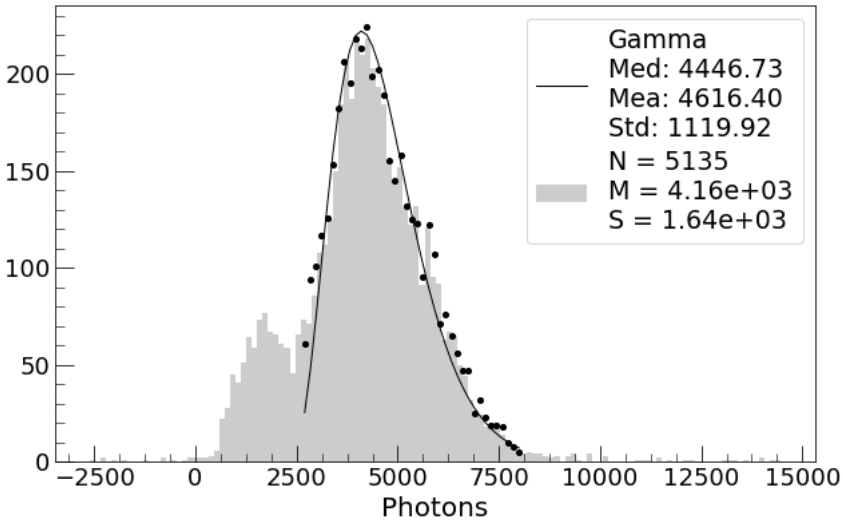

Figure 5.19: Distribution of the light recorded in the X-ray spots with a superimposed Polya fit

After the study of the light intensity for the different gas mixtures, the collective trend has been fit with an exponential. The results in a semilog axis plot is as expected a straight line. For the error, has been used the square root of the number of events contained inside the fit interval.

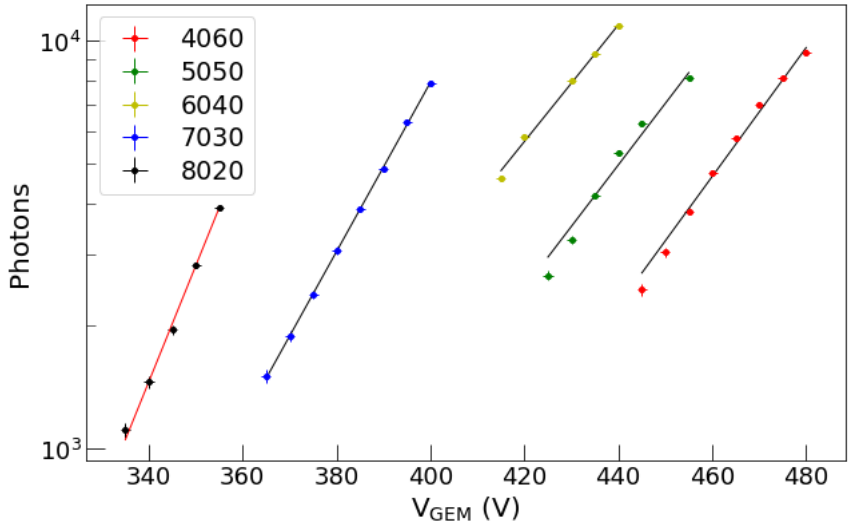

Figure 5.20: Combined plot of the number of photons recorded as a function of V_{GEM} with a superimposed exponential fit

	A	$\delta(V^{-1})$
80/20	$3.1 \cdot 10^{-7}$	$6.5 \cdot 10{-}2$
70/30	$4.0 \cdot 10{-}5$	$4.8 \cdot 10{-}2$
60/40	$5.5 \cdot 10{-}3$	$3.3 \cdot 10{-}2$
50/50	$1.1 \cdot 10{-}3$	$3.5 \cdot 10{-}2$
40/60	$9.0 \cdot 10{-}5$	$3.9 \cdot 10{-}2$

Table 5.1: A and δ values from γ vs V_{GEM} exponential fit

	A(nA)	$\delta(nA/V)$
70/30	$6.62 \cdot 10^{-3}$	0.026
60/40	$8.17 \cdot 10^{-3}$	0.023
50/50	$1.17 \cdot 10^{-3}$	0.026
40/60	$1.94 \cdot 10^{-6}$	0.038

Table 5.2: A and δ values from I_{G3D} vs V_{GEM} exponential fit

	A	$\delta(V^{-1})$
70/30	22.82	0.026
60/40	28.36	0.023
50/50	8.25	0.026
40/60	$6.55 \cdot 10^{-3}$	0.038

Table 5.3: A and δ values from Gain vs V_{GEM} exponential fit

5.6 ORANGE Light-yield

To compute correctly the light-yield for every gas mixture, a factor of normalization must for the electronic gain be computed, and the electron ion pair energy (W_i) must be taken into account. We know $W_i(He) = 41eV$ and $W_i(CF_4) = 54eV$ [18]. For $HeCF_4$ gas mixtures used in our experiments, from the weighted mean of the two quantities we obtained the W_i for every gas mixtures:

Gas mixture	$W_i(eV)$
70/30	44.9
60/40	46.2
50/50	47.5
40/60	48.8

Table 5.4: W_I for gas mixtures

Once the W_i is computed for the gas, we obtain N_e the total number of electron produced per X-ray impinging on the target as:

$$N_e = \frac{5900eV}{W_i} \cdot G_e \tag{5.1}$$

where G_e is the electronic gain for every gas mixture as a function of voltage applied .

The figure 5.21 shows the photons and electrons trend as a function of voltage applied to GEM. Datapoints should superimpose on each other; the distance between two sets could be caused by different gas mixing systems used for the acquisition with X-ray tube and with the ORANGE prototype.

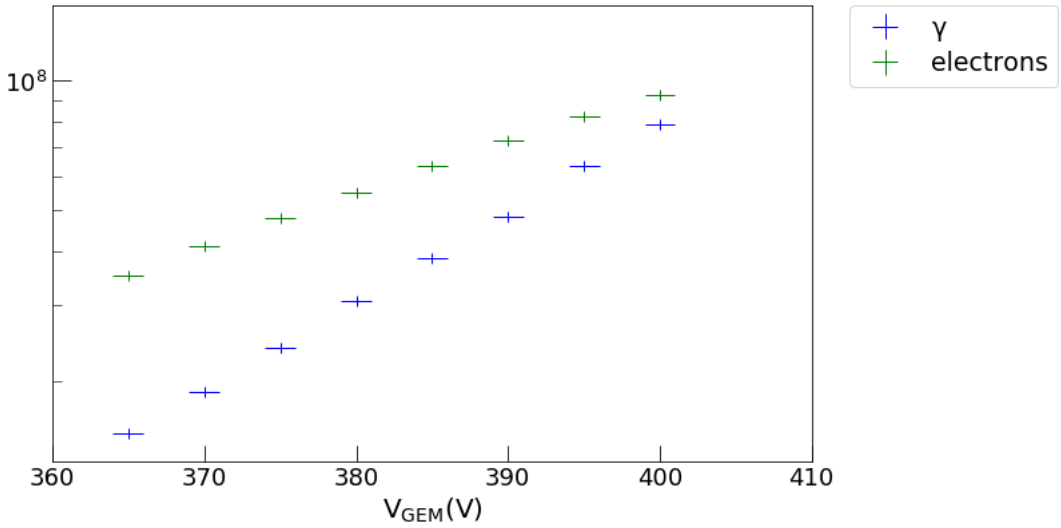

Figure 5.21: γ and electron number as a function of V_{GEM} for 70-30 gas mix

By exponential fit of photons vs V_{GEM}, the number of photons at V_{GEM}=400V was extrapolated. Plotted as a function of mix ratio, it shows the expected trend.

Mix ratio	Photons
2/3	$3 \cdot 10^2$
1	$1 \cdot 10^3$
3/2	$3 \cdot 10^3$
7/3	$8 \cdot 10^3$

Table 5.5: Photons at 400 V vs mix ratio

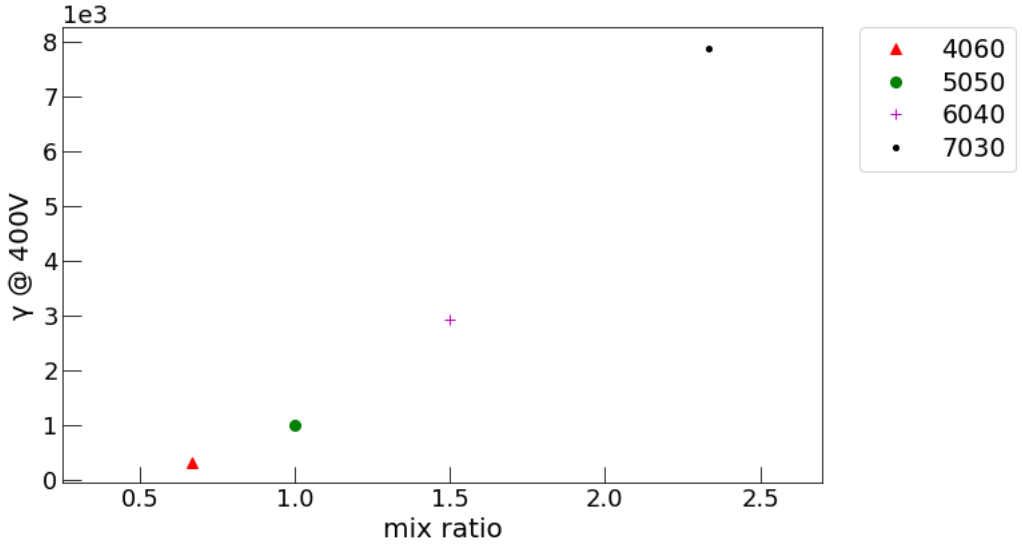

Figure 5.22: Number of photons at V_{GEM}=400V as a function of mix ratio

From the available data and, where necessary with extrapolation from exponential fit, the number of electrons at V_{GEM}=400V .was computed. Plotted as a function of mix ratio, it shows the expected trend.

Mix ratio	Electrons
2/3	$4 \cdot 10^6$
1	$2 \cdot 10^7$
3/2	$4 \cdot 10^7$
7/3	$9 \cdot 10^7$

Table 5.6: Electrons at 400 V vs mix ratio

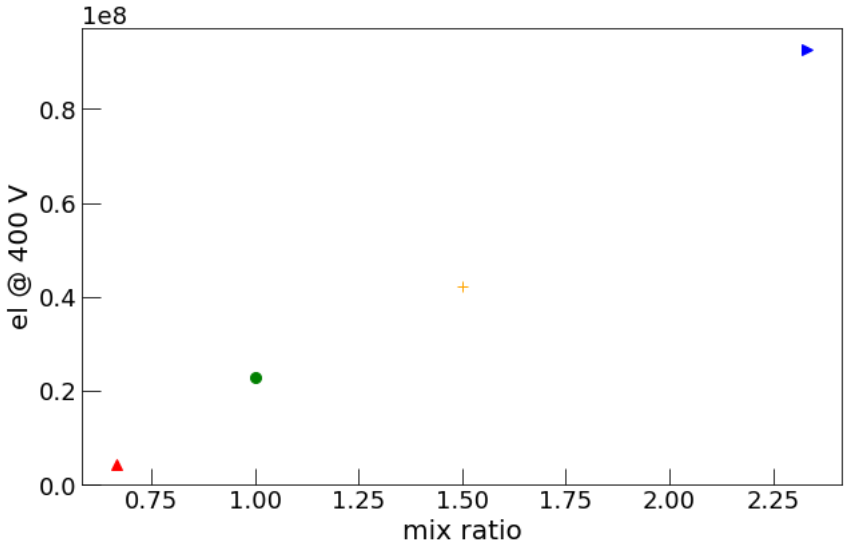

Figure 5.23: Number of electrons at V_{GEM}=400V as a function of mix ratio

Lastly, the total number of photon produced in the gas for every gas mixtures was divided for the total number of electrons to obtain the light-yield, defined as:

$$lightyield = \frac{N_\gamma}{N_e} \tag{5.2}$$

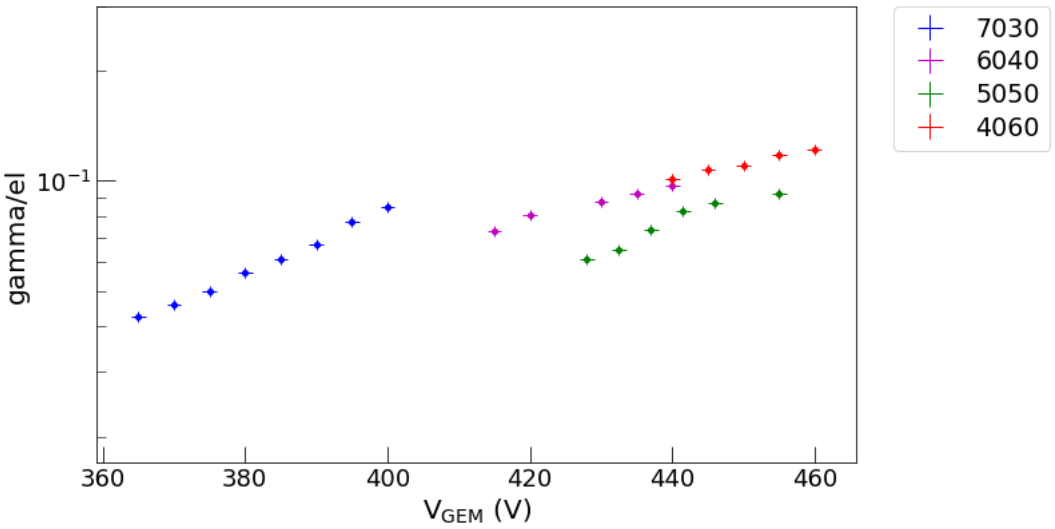

Figure 5.24: Combined plot of light yield as a function of V_{GEM}

In our experimental setup the lens was placed at a distanced of 20 cm

from the last GEM in order to obtain a de-magnification

$$\delta = (\frac{d}{f}) - 1 = 7 \tag{5.3}$$

to image the whole GEM surface on the$13.3mm \times 13.3mm$ sensor. In this configuration,each pixel looked at an effective area of $50 \times 50\mu m^2$. The fraction of the light collected by the lens could be evaluated as

$$\Omega = \frac{1}{(4(\delta + 1) \times a^2)} \simeq 1.0 \times 10^3 \tag{5.4}$$

where $a = 0.95$ and and $f = 25mm$ are, respectively, the aperture and the focal length provided by he Schneider lens used.

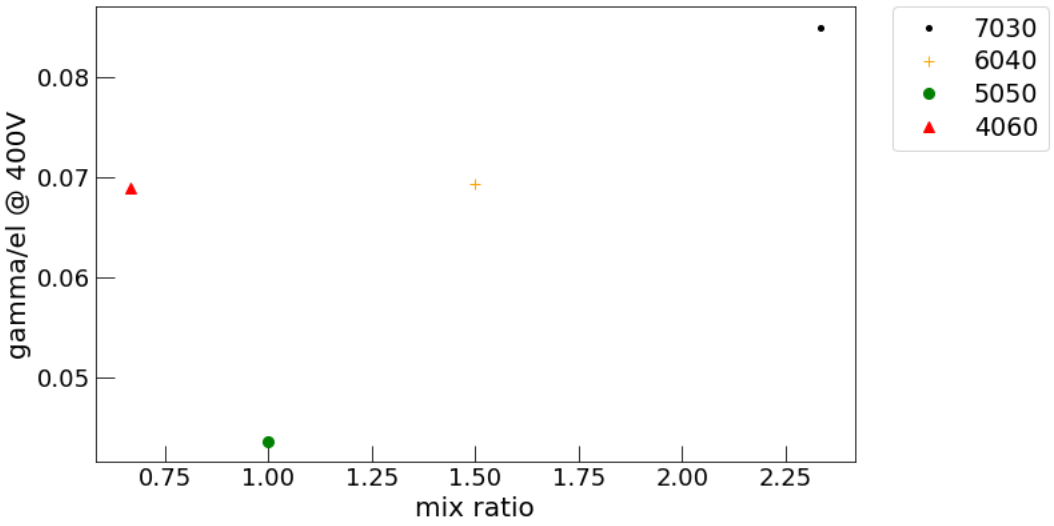

Figure 5.25: Light yield for $V_{GEM} = 400V$ as a function of mix ratio

Mix ratio	γ/elratio
2/3	$7 \cdot 10^{-2}$
1	$4 \cdot 10^{-2}$
3/2	$7 \cdot 10^{-2}$
7/3	$8 \cdot 10^{-2}$

Table 5.7: γ/el ratio at 400 V

The ratio $\frac{N_\gamma}{N_e}$, taken into account the factor Ω, is order $\simeq 10^{-2}$, $\simeq 10^{-1}$ as a function of the voltage applied to the GEM; the light yield computed for $V_{GEM} = 400V$ is between $4 \cdot 10^{-2}$ for 50-50 mix and $8 \cdot 10^{-2}$ for 70-30 mix, as shown in fig: 5.25

The 40-60 mix datapoint is not perfectly aligned to the trend, because of modified experimental conditions during acquisition with x ray tube(different fluxmeter and different condition on the gas mixtures). The photons vs mix ratio(see fig: 5.27) and electrons vs mix ratio dataset were fitted with exponential and for the electrons, the 40-60 data point was extrapolated (see fig: 5.26).

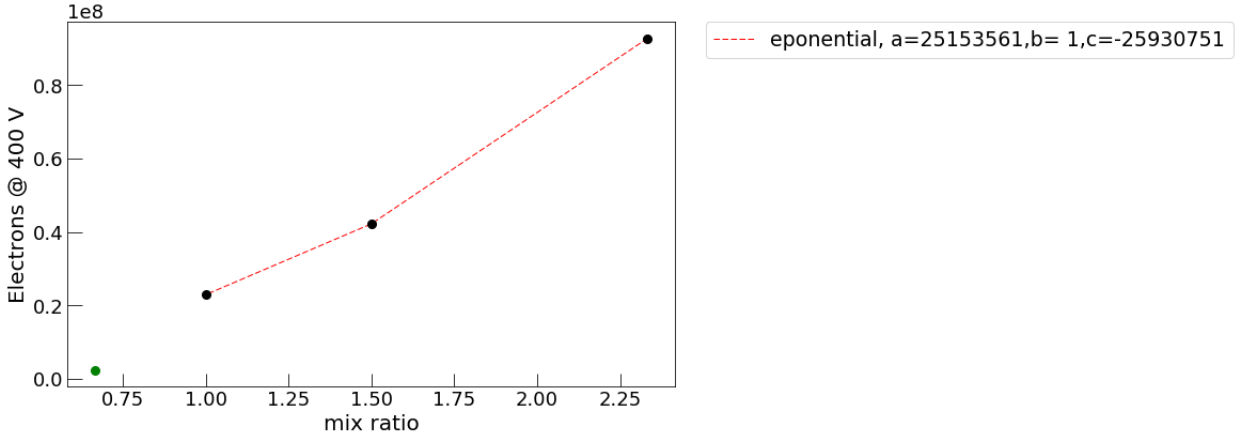

Figure 5.26: Exponential fit of electrons at $V_{GEM} = 400V$ as a function of mix ratio, with extrapolated point (green)

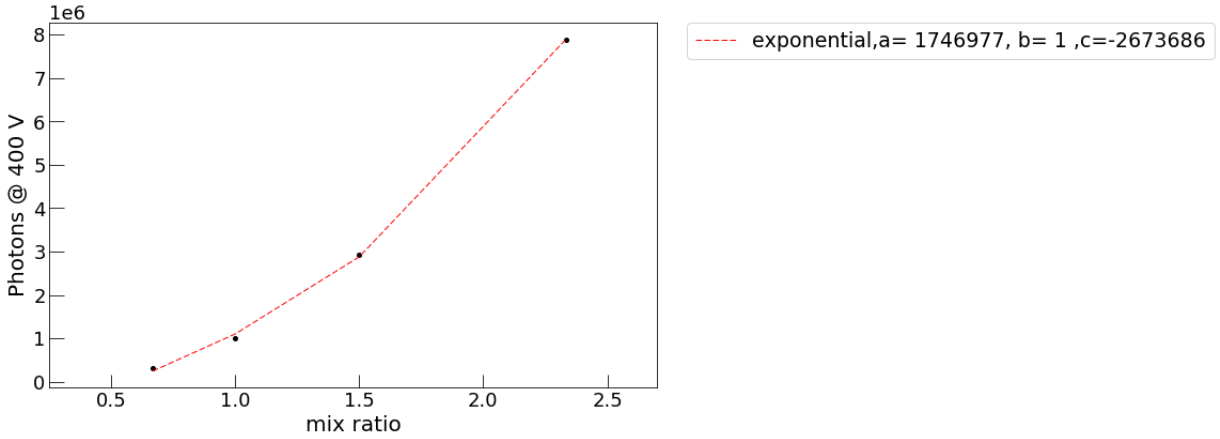

Figure 5.27: Number of photons at $V_{GEM} = 400V$ as a function of mix ratio with exponential fit

To evaluate the expected trend for all datapoint, including 40-60 mix, ratio between the fitted function was plotted. The most probable value for 40-60 datapoint is expected to be 0.2, compared to 0.7 obtained in our experiment, and explained with above-mentioned modified experimental conditions.

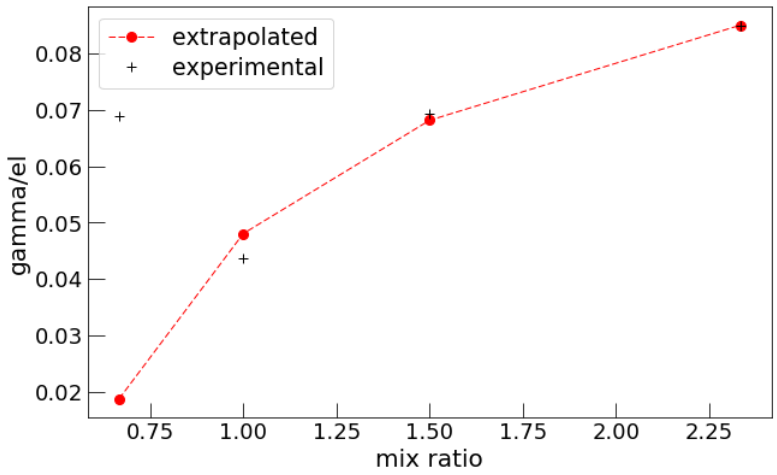

Figure 5.28: Combined plot showing experimental and extrapolated datapoints comparison

5.7 Energy resolution

Another important parameter to be studied is sensitivity of the device to the energy released in the gas. The light collected by the CMOS sensor is expected to be proportional to the energy released, due to an increase of the primary charge density, hence a larger avalanche processes and ionization in the gas, so the number of photons resolution is equivalent to the released energy resolution.
Thus, for every gas mix the number of photons as a function of V_{GEM} has been evaluated, hence the resolution defined as the ratio of Polya standard deviation and the mean number of photon for every acquisition, as returned from the Polya fit.

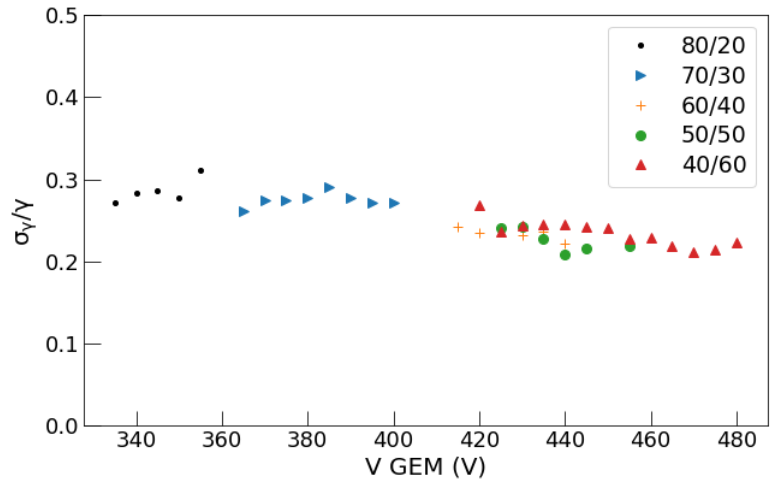

Figure 5.29: Number of photons resolution as a function of V_{GEM}

Then, for every mix the resolution mean value as a function of gas mix has been computed.

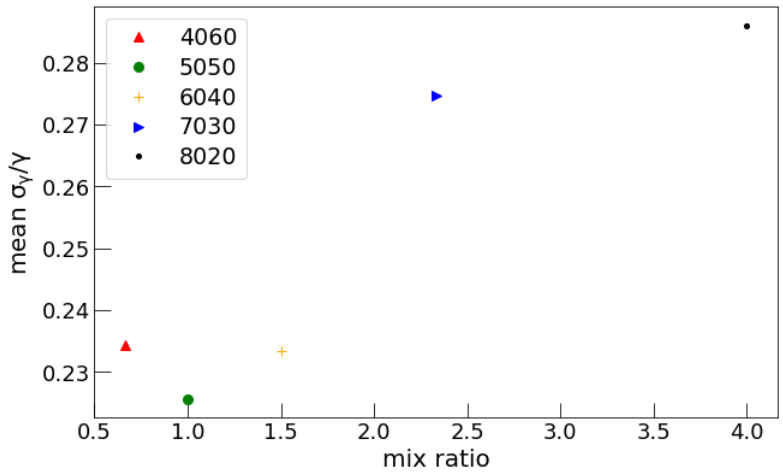

Figure 5.30: Mean photons resolution as a function of gas mixture ratio

50-50 mix offers best resolution; however 60-40 and 70-30 could be consider more suitable to experimental task due to more stability in data taking, and less subject to spark and overcurrent because of the larger amount of CF_4.

Conclusions

The optical readout of triple-GEM system has proved to provide very precious informations to reconstruct tracks of photoemission in the gas detector. Thanks of its high sensitivity and granularity, the use of CMOS sensor to collect the photons, allows to reach a very high level of accuracy.

In this thesis I describe the work and the measurements needed to optimize an optically readout Triple GEM device, and to evaluate the detector light-yield. By means of triple GEM prototype, built in the clean room of the Physics Department of "La Sapienza" University, the first tests were carried out with an x ray tube have been analyzed to calculate the electronic gain for every gas mixture used. The current collected on the third GEM used as electrode, was studied as a function of the voltage applied to the GEMs.
Then, comparing the data with ones obtained in previous experiments conducted at Frascati National Laboratories, the total gain for every gas mixtures was determined.
After the electronic gain, the prototype was used to study the photoemission in the gas mixtures and the related light yield by means of CMOS sensor.
An algorithm based on the Hough transformation was written and the readout images were analyzed. The most probable radius for the track was found to be 8 pixel; the effective scale of the CMOS sensor is known to be $50\mu m$ per pixel, so the actual dimension of the track was evaluated.
By means of the algorithm, the light content of the images was measured.
The energy resolution is between 22% and 28%, as expected from other studies; 60-40 and 70-30 mix are confirmed to be more suitable for future and improved experiments.
Lastly, the total number of photon for every gas mixture was divided by the total electronic gain and the light yield was evaluated, giving values of order 10^{-2} as expected.
The progress of technology connected with this type of system, has brought and will bring more and more important results. The results reported in this thesis work permit to find, to date, the better configuration for an innovative and versatile detector.

Bibliography

[1] G Capon. "W. Blum, L. Rolandi-Particle detection with drift chambers". In: *Il Nuovo Cimento A (1971-1996)* 108.9 (1995), pp. 1161–1162.

[2] Pinci D. *A triple-GEM detector for the muon system of the LHCb experiment*. Tech. rep. 2003.

[3] Carlo Dall'Alba. *Sensori di immagine CCD e CMOS*. `http://tesi.cab.unipd.it/40910/1/Sensori_d'immagine_CCD_e_CMOS.pdf`. 2012.

[4] C. Dionisi E. Longo. *Dispense del corso di Fisica Nucleare e Subnucleare*. `http://www.roma1.infn.it/people/longo/fnsn/testo.html`.

[5] G. Audi et al. "The NUBASE Evaluation of Nuclear and Decay Properties". In: *Nuclear Physics A* 729.1 (2003), pp. 3–128.

[6] G Bencivenni et al. "Measurement of GEM parameters with X-rays". In: *IEEE Transactions on Nuclear Science* 50.5 (2003). DOI: `10.1109/TNS.2003.818234`.

[7] FAF Fraga et al. "CCD readout of GEM-based neutron detectors". In: *Nuclear Instruments and Methods in Physics Research Section A: Accelerators, Spectrometers, Detectors and Associated Equipment* 478.1 (2002), pp. 357–361.

[8] MMFR Fraga et al. "The GEM scintillation in He–CF 4, Ar–CF 4, Ar–TEA and Xe–TEA mixtures". In: *Nuclear Instruments and Methods in Physics Research Section A: Accelerators, Spectrometers, Detectors and Associated Equipment* 504.1 (2003), pp. 88–92.

[9] Esam M. A. Hussein. *Handbook on radiation probing, gauging, imaging and analysis*. Springer, 2003.

[10] FA Jenkins. *Fundamental of Optics*. McGraw-Hill, 1957.

[11] M. Marafini et al. "High granularity tracker based on a Triple-GEM optically read by a CMOS-based camera". In: *JINST* 10.12 (2015), P12010. DOI: 10.1088/1748-0221/10/12/P12010.

[12] *Insulated-gate Field-effect Transistors (MOSFET)*. 2016.

[13] Laboratori Nazionali di Frascati. http://www.lnf.infn.it/.

[14] *ORCA-flash4.0*. Tecnical Note.

[15] D. Pinci. *Rivelatori a Gas-INFN Roma*. http://www.roma1.infn.it/people/rahatlou/labhep/material/Gas-LabIV.pdf. retrived on 2016.

[16] F. Sauli. "GEM: A new concept for electron amplification in gas detectors". In: *Nuclear Instruments and Methods in Physics Research Section A: Accelerators, Spectrometers, Detectors and Associated Equipment* 386.2 (1997), pp. 531–534.

[17] Linda Shapiro and George Stockman. *Computer Vision*. Prentice-Hall Inc., 2001.

[18] Archana Sharma. *Properties of some gas mixtures used in tracking detectors*. http://www.slac.stanford.edu/pubs/icfa/summer98/paper3/paper3.pdf.

[19] Ben G Streetman and Sanjay Banerjee. *Solid state electronic devices*. Vol. 4. Prentice Hall New Jersey, 2000.

[20] Albert H Titus and Vamsy P Chodavarapu. *CMOS Photodetectors*. INTECH, 2011.